EES Catalysis

REVIEW ARTICLE

View Article Online
View Journal | View Issue

Cite this: *EES Catal.*, 2023, 1, 590

Microkinetic studies for mechanism interpretation in electrocatalytic CO and CO_2 reduction: current and perspective

Xiaofei Lu, Keisuke Obata and Kazuhiro Takanabe *

Microkinetic analysis can establish the relationship between the atomic-level reaction mechanism and macroscopic observables, such as reaction rates, product selectivity, Tafel slope, reaction order, isotopic effect, and apparent activation energy, at given operating conditions. This relationship is essential in the rational design of electrocatalysts and reactor configurations. In recent years, microkinetic analysis, particularly Tafel and reaction order analysis, has seen significant advancements in its application for interpreting reaction mechanisms in electrocatalytic CO and CO_2 reduction. This review summarizes the progress in understanding the complex kinetic processes through theoretical microkinetic simulation modeling and experimental measurements. However, the reaction mechanisms derived from microkinetic analysis are disputed, complicating efforts to design electrocatalysts. This review analyzes the discrepancies in the literature and elucidates deeper insights into experimental discrepancies. The importance of local reaction environments in the intrinsic kinetic behavior of electrocatalysts is highlighted. The report also discusses the challenges and limitations of microkinetic analysis. Finally, the review suggests some perspectives on future investigations. Overall, this review is expected to provide new insights, critical interpretation, and guidance for the future development of microkinetic measurements and analysis.

Received 10th April 2023,
Accepted 24th May 2023

DOI: 10.1039/d3ey00079f

rsc.li/eescatalysis

Broader context

Electrochemical CO_2 reduction powered by renewable energy offers a sustainable and cost-effective approach to convert harmful CO_2 emissions into valuable chemicals and fuels, reducing the dependency on fossil fuels and contributing to the development of a circular carbon economy. Microkinetic analysis plays a crucial role in the design and optimization of catalytic systems, which allows for the determination of the reaction pathways and the identification of the rate-determining step involved in CO_2 electroreduction. Nevertheless, the reaction mechanisms derived from microkinetic analysis remain debatable, impeding the establishment of design guidelines for effective catalysts and the optimization of reaction conditions. This review attempts to summarize the recent advancements in the understanding of complex kinetic processes through theoretical microkinetic simulation modeling and experimental measurements. The discrepancies in the literature are analyzed, highlighting the significance of local reaction environments in the intrinsic kinetic behavior of electrocatalysts. Furthermore, it discusses the challenges and limitations of microkinetic analysis in electrochemical CO_2 reduction. Finally, operando spectroscopies as complementary tools are proposed, and strengthening the connection between experiments and computation is emphasized to increase its accuracy and reliability in reaction mechanism interpretation.

1. Introduction

The electrocatalytic reduction of CO and CO_2 ($CO_{(2)}$) may offer an alternative route to produce carbonaceous fuels and chemicals in decarbonized societies, especially with the decrease in renewable electricity prices.[1–3] Therefore, huge research efforts have been dedicated to this direction in the last few decades, demonstrating the potential of producing CO, formate, or hydrocarbons *via* electrocatalytic $CO_{(2)}$ reduction.[4–7] However, despite the added motivation of the gas-diffusion electrode (GDE), these processes still suffer from low efficiency and require the development of active and selective electrocatalysts for any large-scale implementation.[8–11] Unfortunately, interpreting the atomic-level reaction mechanisms remains controversial due to the involvement of multiple electron and proton transfers, hampering the establishment of robust design principles for electrocatalysts.

Microkinetic modeling is a powerful tool for addressing rate-determining steps (RDS) and detailed reaction pathways, both

Department of Chemical System Engineering, School of Engineering, The University of Tokyo, 7-3-1 Hongo, Bunkyo-ku, Tokyo 113-8656, Japan. E-mail: takanabe@chemsys.t.u-tokyo.ac.jp

of which are explanatory and predictive in rational catalyst design.[12–18] For example, microkinetic analysis using density functional theory (DFT) calculations provides a deeper understanding of why Au and Ag are at the top of the experimentally obtained volcano trend for CO evolution during electrocatalytic CO_2 reduction, revealing the moderate binding affinity of the adsorbed carboxylate (*COOH) on Au and Ag.[19–22] Additionally, it distinguishes Cu from other elements as the only metal to go beyond C1 products efficiently in electrocatalytic CO_2 reduction.[4,23] Furthermore, Sargent and his colleagues developed a machine-learning-accelerated, high-throughput DFT framework to identify Cu–Al alloys as promising electrocatalysts for C_2H_4 production.[24] Despite the wide application of DFT-based microkinetic modeling, using it as a quantitative predictive tool is challenging.[25] Therefore, enhancing the connections between computation and experimental observables is essential to increase the effectiveness of microkinetic modeling.

Microkinetic analysis from experiments is essential for creating precise DFT-based microkinetic models for the active site and its environment. Tafel analysis is one of the most common experimental techniques used to understand the RDS in electrocatalytic CO_2 reduction.[26,27] In the classical analysis, the experimentally observed Tafel slope is compared with the theoretically derived slope to identify the corresponding RDS. However, this method has several assumptions, including steady-state reactions and no mass transportation limitations under reaction conditions, the constant assumptions (0 or 1) of intermediate surface coverage, and an electron transfer coefficient of 0.5.[28–31] To point out the RDS, additional methods are necessary, as different proposed RDS can yield the same identified Tafel slope.[26,27,29] For instance, one electron transfer and proton-coupled electron transfer (PCET) over Ag and Au both yield a Tafel slope of approximately 120 mV dec^{-1}.[26,31,32] Thus, the isotopic effect (hydrogen/deuterium) or operando spectroscopies are necessary to provide deeper insights into the RDS. Moreover, the type of proton donor and CO_2 source must be identified since protons can come from various sources including H_2O, free proton (H^+), and H-containing species (*e.g.*, HCO_3^-); CO_2 can be supplied by gas-phase CO_2 or bicarbonate.[20,31,33] The apparent reaction orders with respect to pH and reactants (*e.g.*, partial pressure of $CO_{(2)}$ ($P_{CO_{(2)}}$) and bicarbonate concentration ($c_{HCO_3^-}$)) can distinguish between them.[34] Temperature dependence can also provide a fingerprint of the reaction pathways. Overall, rigorous microkinetic analysis using Tafel slopes, kinetic isotope effects (KIE), apparent reaction orders, and temperature sensitivity can deconvolve the complexity of interface reactions occurring on the electrode and elucidate the reaction mechanisms, which are highly desired in rational catalyst design.

Up to this point, several issues have arisen in interpreting experimental kinetic data, related to measuring the intrinsic kinetic behavior of catalysts.[26,33,35,36] For example, local environments and experimental designs can significantly affect the experimental results, which can, in turn, mislead the mechanistic elucidation.[37–42] Moreover, some assumptions have limitations. The theoretically derived slopes, for instance, generally assume an extreme coverage of the adsorbed species (θ = 0 or 1).[43,44] However, several studies have claimed to observe some key intermediates *via* joint spectroscopic/DFT techniques,[45–47] including the negatively charged CO dimer on Cu during CO reduction,[48] adsorbed CO and CH_x on Cu-based catalysts,[49–51] and proposed COOH intermediate over polycrystalline Ag (pc-Ag)[52] during CO_2 reduction. Additionally, the charge transfer coefficient is always assumed to be 0 or 0.5 for elementary steps, although, in practice, it is a function of both overpotentials and reorganization energy.[29,30] Therefore, revisiting microkinetic analysis and understanding its limitations during $CO_{(2)}$ reduction are of crucial in elucidating atomic-level reaction mechanisms.

This review mainly focuses on the development, challenges, and limitations of microkinetic analysis during electrocatalytic $CO_{(2)}$ reduction. Firstly, it reviews the DFT-based microkinetic modeling of various products, such as CO, formic acid, CH_4, and C_{2+}. It addresses the theoretically derived Tafel slopes and reaction orders under the assumption of different RDSs. Secondly, it summarizes and discusses the experimentally observed parameters (*e.g.*, Tafel slopes, reaction orders, and kinetic isotopic effects) and corresponding reaction mechanisms over various electrocatalysts in electrocatalytic $CO_{(2)}$ reduction. Special attention is given to the discussions of the reported discrepancies in the literature. Moreover, the existing challenges and limitations in the microkinetic analysis are interpreted from different aspects, such as intrinsic kinetic measurements, dynamically restructured catalyst, the complexity of electrolyte effects, intermediate surface coverage assumption, and electron transfer coefficient. Finally, this review provides an outlook on the future development of kinetic analysis in rational catalyst design. It implies the importance of operando spectroscopies and computational methods as complementary tools in microkinetic modeling. This review provides deeper insights into microkinetic analysis in electrocatalytic $CO_{(2)}$ reduction and emphasizes the importance of these complementary tools for future research.

2. DFT-based microkinetic simulation of electrocatalytic $CO_{(2)}$ reduction

The pioneering work by Hori *et al.* examined a variety of metal electrodes for the electrocatalytic CO_2 reduction reaction, having stimulated the development of heterogeneous catalysts in this field.[53–57] Among them, copper is a unique catalyst sitting at the top of the "volcano" plot for electrocatalytic CO_2 reduction, in which both CO- and formate-paths prevail, yielding a variety of CO_2-reduction products.[4] In contrast, there have been several elements reported to achieve exclusive production of single products (*e.g.*, CO, HCOOH). More specifically, p-block electrodes, such as indium or tin, selectively produce formate while keeping the concurrent hydrogen evolution reaction (HER) silent.[58–62] In addition, although the metals in groups 8–10 of the periodic table favor the HER over the CO_2 reduction routes, gold and silver metal electrocatalysts direct the reaction toward the CO route selectively, achieving a faradaic efficiency

toward CO (FE_{CO}) greater than 90%.[32,33,63,64] Interestingly, DFT calculations could interpret the activity-selectivity map by quantifying the free energies of reaction intermediates, *e.g.*, *COOH, *CO, and *OCOH species, in agreement with the experimentally obtained results. These findings validate the reliability of DFT-based microkinetic modeling in electrocatalytic CO_2 reduction, where the active site and its electrochemical environment have been taken into account due to advancements in the computation.[37,65–72] The widespread success has made computational methods a routine practice as quantitative predictive tools.

This section reviews the recent development of DFT-based microkinetic simulation of electrocatalytic $CO_{(2)}$ reduction, mainly focusing on key intermediates (descriptors) and proposed reaction pathways. Moreover, the theoretically calculated kinetic parameters (*e.g.*, Tafel slope, reaction order, and KIE) are also summarized by assuming different RDSs in proposed reaction pathways during electrocatalytic $CO_{(2)}$ reduction.

2.1 Key intermediates (descriptors) and reaction pathways for C_1 formation

Although the reaction pathways of CO and formic acid/formate formation ($HCOOH/HCOO^-$) over different catalysts remains debated, the key intermediates (descriptors) have been well-defined by recent calculation studies. Chan and co-workers depicted a unified mechanistic picture of electrocatalytic CO_2 reduction toward CO on transition metals (TMs), molecular complexes (*e.g.*, phthalocyanine (Pc)), and metal–nitrogen-doped carbon catalysts (MNCs) by using the Newns–Andersen model, where the effects of the adsorbate–field interactions for all the intermediates were taken into account.[73] The general kinetic activity of CO evolution was determined by two activity descriptors, namely the free energy of adsorption (ΔG) of CO_2 and COOH, as shown in Fig. 1a and b. Fig. 1a exhibited the unified activity volcano for the CO evolution on both TM and MNC catalysts, and the maximum theoretical activity appeared when both ΔG_{CO_2} and ΔG_{COOH} were close to 0 eV. Moreover, the RDS could be identified at any given potential using computed $*CO_2$, *COOH, and *CO free energies. More specifically, CO_2 adsorption was the RDS when the points appeared above the parity line (*e.g.*, TM), while *COOH formation was the RDS if the points were below the line (*e.g.*, NiN_x and FeN_x). They found that on MNCs, electron transfer to CO_2 was facile. Moreover, *CO desorption could be the RDS with very negative adsorption energies (Fig. 1b), where the surface was poisoned by *CO (*e.g.*, Pd and Pt). Feaster *et al.* used a DFT-based microkinetic

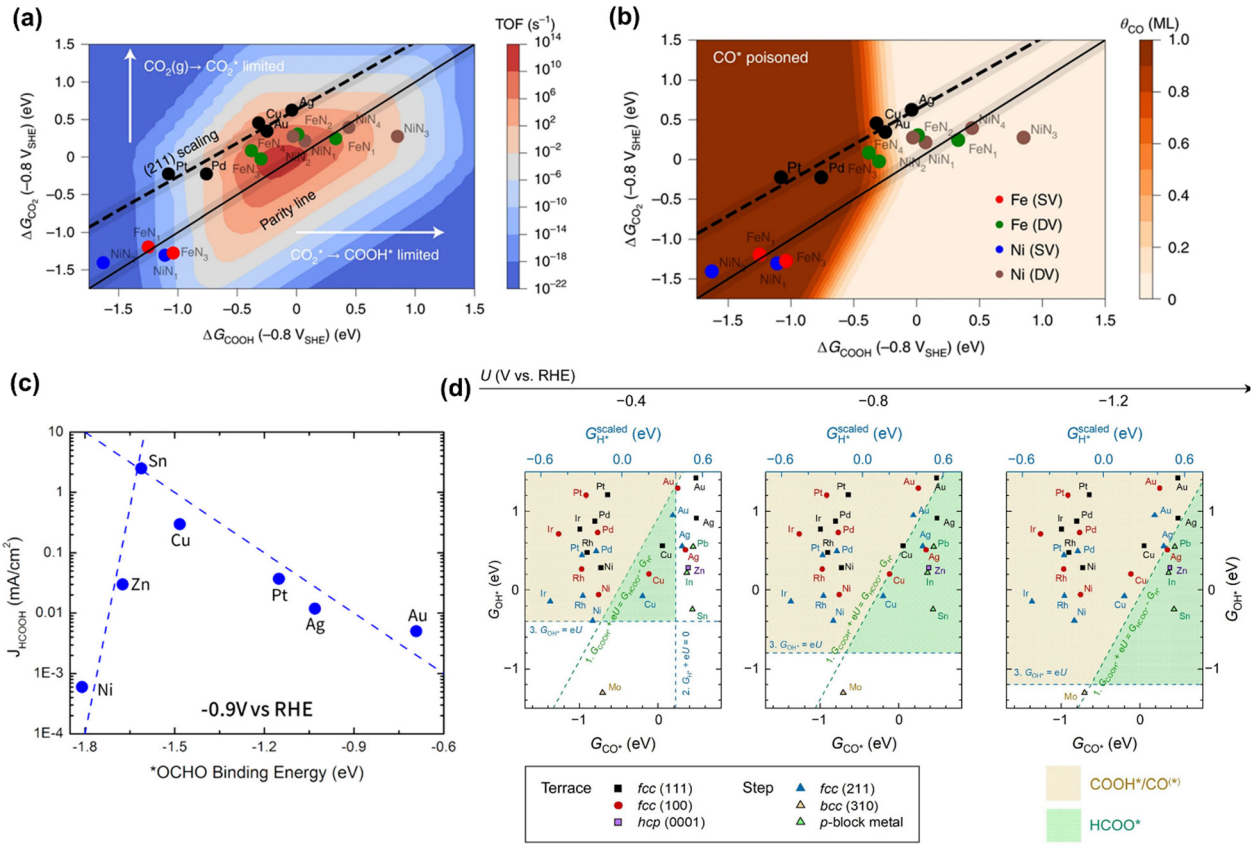

Fig. 1 (a) The trends in the binding of key intermediates (ΔG_{CO_2} and ΔG_{COOH}) and corresponding rate map at −0.8 V *versus* standard hydrogen electrode (SHE) and pH 2 for CO evolution over TMs and MNCs. (b) CO coverage map (θ_{CO}) in monolayers (ML) with the same points showing which surfaces are poisoned by CO. Reproduced with permission.[73] Copyright 2021, nature publishing group. (c) The trends in binding *OCHO for formic acid production over TMs. Reproduced with permission.[74] Copyright 2017. (d) The potential-dependent selective regions for formate, CO, and H_2 were plotted by combining descriptor (ΔG_{CO}, ΔG_{OH}) maps. Reproduced with permission.[75] Copyright 2020, from Elsevier.

model to describe the experimentally observed trend of formate production over TMs, showing why Sn was the best-known metal electrocatalyst (Fig. 1c). The *OCHO binding energy was singled out as the most important descriptor.[74] The potential-dependent selective regions for formate, CO, and H_2 were plotted by combining descriptor (ΔG_{CO}, ΔG_{OH}) maps, as shown in Fig. 1d. The dashed green line represented the thermodynamic boundary condition defined by $\Delta G_{COOH} = \Delta G_{HCOO}$.[75]

Additionally, the nature of the electrogenerated reactive nucleophilic species were also identified as important descriptor to determine the selectivity between CO and HCOOH/$HCOO^-$ during CO_2 reduction.[76–78] For metal tetraphenylporphyrin (MTPP),[76] the electrogenerated metal-hydride or phlorin-hydride (M: In, Sn, Rh, Cd, Ga, and Pd) could attack the carbon of the CO_2 to form C–H bond, which resulted in the formation of HCOOH/$HCOO^-$.[79] On the contrary, the reduced metal-centers (*e.g.*, Fe, Co, Ni) triggered the formation of the metal–carbon bond with CO_2, which then gave rise to the formation of CO.[76] Similarly, it also has been reported that the thermodynamically generated surface adsorbed hydrogen on Pd could significantly decrease the overpotential of formate production in aqueous bicarbonate solutions.[77] And the product distributions on PC–Cu and Au were shifted from CO to formate at low overpotentials after chemical modification with a poly(4-vinylpyridine) (P4VP) layer, which was suggested to promote a surface hydride mechanism for formate formation on both electrodes.[80]

2.2 Key intermediates (descriptors) during reaction pathways for CH_4 and C_{2+} formation

CO is demonstrated as a key intermediate on the pathway to CH_4 and C_{2+} compounds during electrocatalytic CO_2 reduction.[57,81] Only copper-based electrocatalysts have been reported to convert CO_2 into CH_4 or C_{2+} products at moderate rates under ambient pressure and temperature, which was rationalized that Cu-based electrodes possess the balanced chemisorption energy of CO and proton (Fig. 2a).[4] Accordingly, this review only focuses on the microkinetic models for CO electroreduction towards CH_4 and C_{2+} on Cu based electrodes.

Nørskov and co-workers developed a first-order absorbate interaction model for CH_4 formation (Fig. 2b), where the proton-electron transfer from *CO to *H-CO was considered

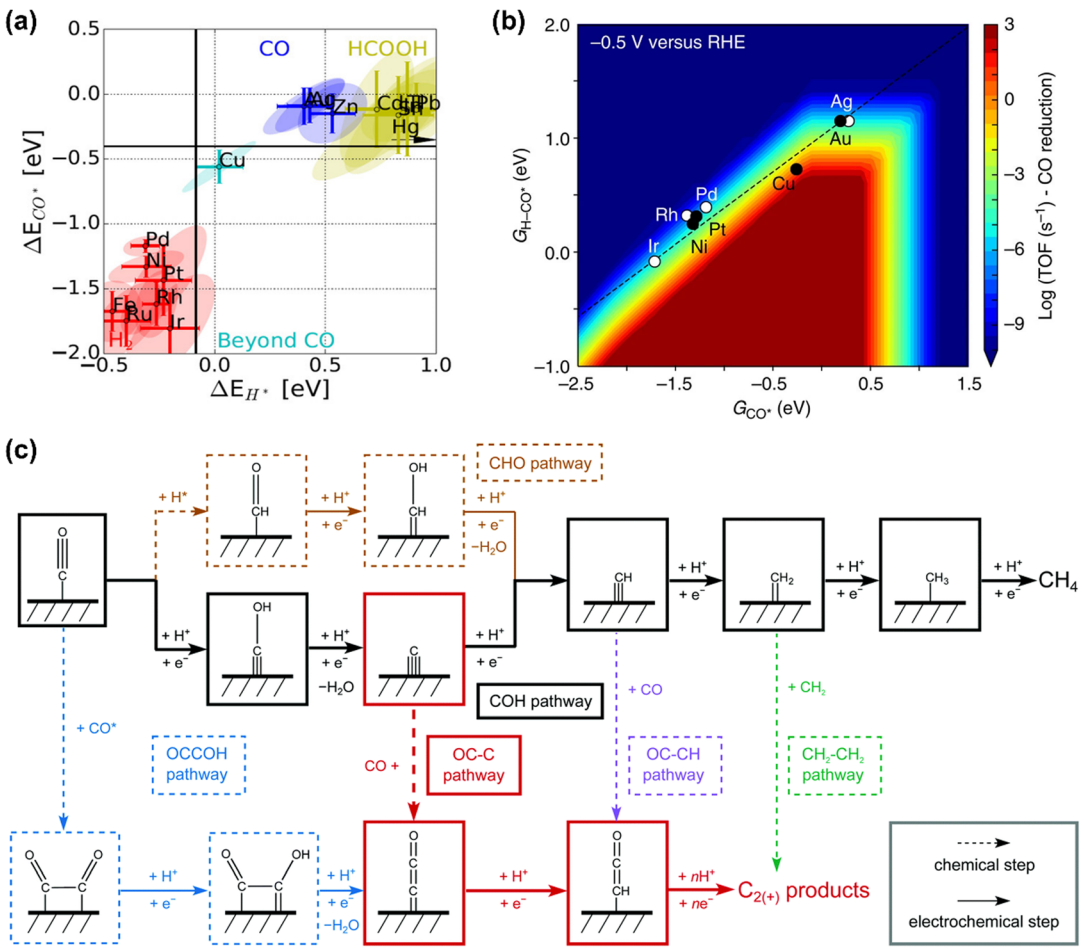

Fig. 2 (a) Metal classification for CO_2 electroreduction. Reproduced with permission.[23] Copyright 2017, Wiley. (b) Rate map at −0.5 V *versus* reversible hydrogen electrode (RHE) for CH_4 formation over Cu. Reproduced with permission.[82] Copyright 2017, Nature. (c) Schematic diagram of reaction steps for C_{2+} over Cu. Reproduced with permission.[84] Copyright 2021, from RSC Publishing.

as RDS for CH_4 formation and the stepped facet was predicted to deliver significantly higher rates than flat facets due to the preferred *CO protonation on the stepped facet.[82] Regarding C_{2+} products, the processes are very complex due to the involvement of multiple proton and electron transfers. Goodpaster *et al.* built microkinetic modeling on Cu(100) to predict ΔG of elementary steps for C_{2+} formation, where the electrochemical potential, solvent, and electrolyte were considered. This model revealed that C–C bond formation occurred *via* CO dimerization at low-applied potential, which shifted to the coupling between adsorbed CO and CHO at high overpotentials.[83] Peng *et al.* also established microkinetic modeling to identify the key steps toward CH_4 and C_{2+} products on Cu(100) (Fig. 2c), where two simple thermodynamic descriptors (ΔG_{C^*} and ΔG_{CO^*}) were proposed. The selectivity between C_{2+} and CH_4 was determined through the energetic difference between barriers for *CCO and *CH formation.[84]

In terms of pH dependence on CH_4 and C_{2+} formation, in Peng's model (Fig. 3a), the dominant pathway for C_{2+} formation was *CO and *C coupling at neutral pH and moderate potential windows (*e.g.*, −0.4 V to −1 V *vs.* reversible hydrogen electrode (RHE)), which shifted to the coupling between *CO and *COH at high pH. For CH_4 formation, it preferred the formation *COH first and then went through a *C intermediate under wider pH and potential windows. Moreover, some other pathways have been proposed for CH_4 (*e.g.*, *CHO pathways) and C_{2+} (*e.g.*, *OC–CH pathway and *CH_2CH_2 pathway).[84] Xiao *et al.* used an implicit solvation model on Cu(111) to interpret the reaction pathways and examine the pH effects, showing that higher pH favored C–C coupling through the dimerization of *CO and the common intermediate *COH was shared by CH_4 and C_2H_4 at neutral pH.[85] Hahn and co-workers also performed microkinetic analysis using a constant-potential model to understand the Tafel slopes and pH dependences on the formation of C_{2+} and CH_4.[86,87] They found that their different rate-limiting steps lead to distinctive potential dependent Tafel slope and pH effects on C_{2+} and CH_4 formation, as shown in Fig. 3b and c, respectively. Clearly, C_{2+} formation at low overpotentials (> −1.4 V *vs.* standard hydrogen electrode (SHE)) was limited by the first proton–electron transfer to the *OCCO using H_2O as proton source at pH = 7 and 13, while the corresponding RDS was shifted to CO dimerization at high overpotentials with increased Tafel slopes. In contrast, H_3O^+ was the predominant proton donor and CO–CO dimerization was the RDS throughout the considered potential range at pH = 3. For CH_4 formation at pH = 13, the RDS shifted from the *CH–OH formation with a Tafel slope of 28 mV dec^{-1} at low overpotentials (> −1.45 V *vs.* SHE) to the *CO–H formation with a Tafel slope of 96 mV dec^{-1} at high overpotential. Reducing the electrolyte pH led to a change of RDS to the first protonation step using H_3O^+ as the proton donor through the investigated potential range.[86] Given the challenge of large

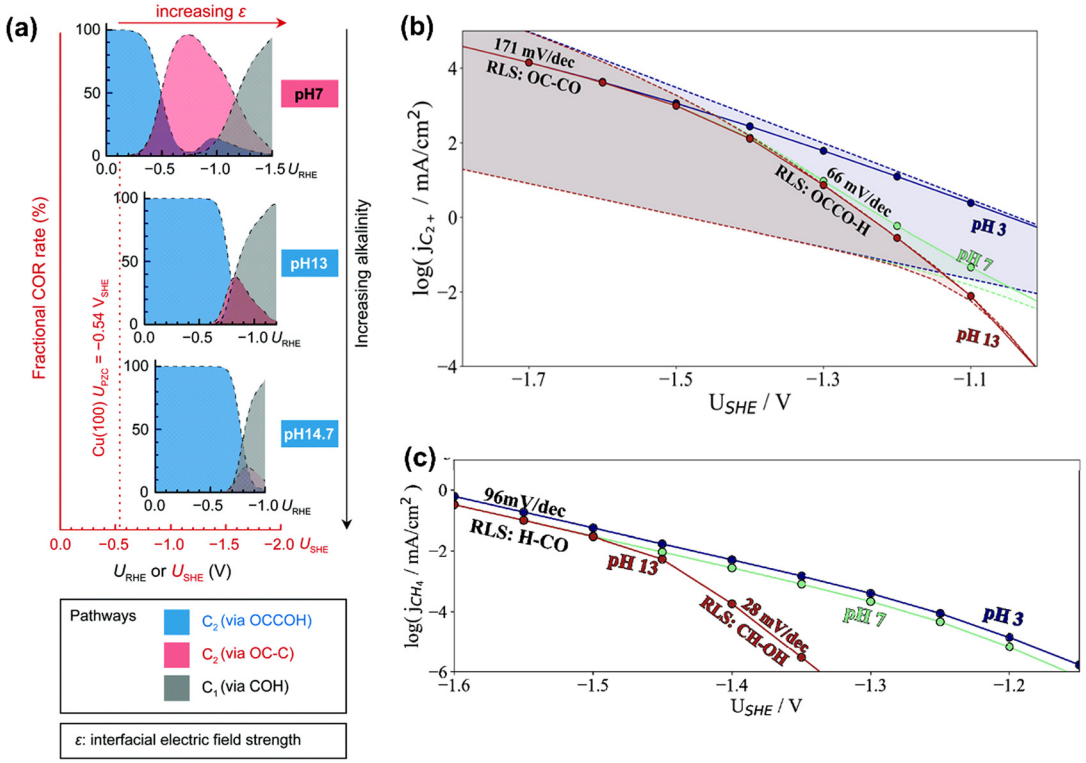

Fig. 3 (a) Product distributions of CO electroreduction on Cu(100) under different bulk pH conditions. Reproduced with permission.[84] Copyright 2021, from RSC Publishing. (b) Simulated current densities using a microkinetic model based on the DFT-calculated energetics on Cu(100). (c) Simulated current densities using a microkinetic model based on the DFT-calculated reaction energetics on Cu(211). Reproduced with permission.[86] Copyright 2022, American Chemical Society.

uncertainties in calculated rates, the theoretical models need to be verified by experimental results.

2.3 Theoretically calculated kinetic parameters

Conventionally, the microkinetic analysis helps to obtain three important physical parameters: the Tafel slope, reaction order, and KIE (hydrogen/deuterium). The Tafel slope (b) has been empirically defined in eqn (1):

$$\eta = a + b\log(j) \quad (1)$$

which relates reaction rates (j) to electrochemical driving force (η). Meanwhile, simple charge-transfer redox reaction kinetics (eqn (2), where O and R denote oxidant and reductant, respectively) are described using the Butler–Volmer eqn (3):[88]

$$O + ne^- \leftrightarrow R \quad (2)$$

$$j = nF\left[k_b^0 a_R \exp\left(\frac{\alpha\eta F}{RT}\right) - k_f^0 a_O \exp\left\{\frac{-(1-\alpha)\eta F}{RT}\right\}\right] \quad (3)$$

where k_b^0 and k_f^0 denote the back and forward rate constant, respectively; a_O and a_R are the concentrations of oxidant and reductant, respectively; α is the transfer coefficient, F is the Faraday's constant, R is the universal gas constant, and T defines the absolute temperature. Eqn (4) and (5) are derived from eqn (3) at equilibrium conditions and high overpotential conditions, respectively:

$$a_R/a_O = k_f^0/k_b^0 \exp\left(\frac{-\eta F}{RT}\right) = K^0 \exp\left(\frac{-\eta F}{RT}\right) \quad (4)$$

$$j = -nF\left[k_f^0 a_O \exp\left\{\frac{-(1-\alpha)\eta F}{RT}\right\}\right] \quad (5)$$

Hence, the empirical Tafel slope can be obtained by combining eqn (1), (4) and (5) based on the mean-field approximation. Based on the theoretical understanding of electrocatalytic CO_2 reduction, all possible elementary steps were simplified in Fig. 4, with assumptions that the intermediate surface coverage

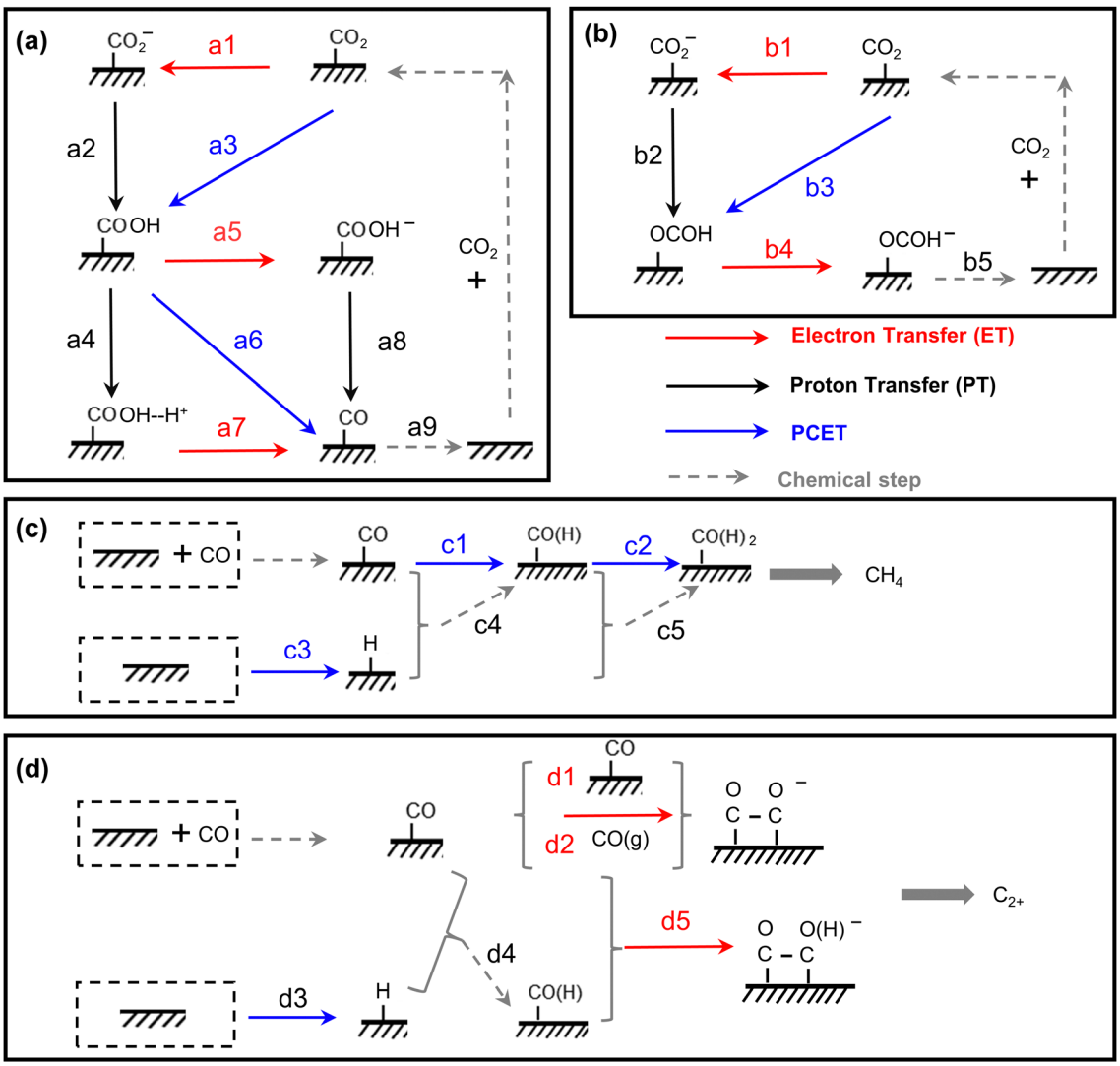

Fig. 4 The scheme of all possible reaction pathways for various products in electrocatalytic CO_2 reduction. Formation of (a) CO, (b) $COOH^-$, (c) CH_4, and (d) C_{2+}.

Table 1 Reaction kinetic parameters under the assumption of various rate-determining steps (RDSs) for CO evolution during electrocatalytic CO_2 reduction

Proton donor		RDS	Tafel mV dec^{-1} [a]		Reaction order H^+	Reaction order P_{CO_2}	Reaction order $c_{HCO_3^-}$	KIE
H_2O	Type 1	$CO_2 + e^- + M \rightarrow M\text{-}CO_2^-$ (a1)	$2.3RT/F(\alpha-1)$	118	0	0–1	0	N
		$M\text{-}CO_2^- + H_2O \rightarrow M\text{-}COOH + OH^-$ (a2)	$2.3RT/F$	59	0			Y
		$M\text{-}COOH + e^- \rightarrow M\text{-}COOH^-$ (a5)	$2.3RT/F(\alpha-2)$	39	1			N
		$M\text{-}COOH^- \rightarrow M\text{-}CO + OH^-$ (a8)	$2.3RT/2F$	30	1			Y
		$M\text{-}CO \rightarrow CO + M$ (a9)	$2.3RT/2F$	30	2			N
	Type 2	$CO_2 + H_2O + e^- + M \rightarrow M\text{-}COOH + OH^-$ (a3)	$2.3RT/F(\alpha-1)$	118	0			Y
		$M\text{-}COOH + H_2O \rightarrow M\text{-}COOH\text{–}H^+ + OH^-$ (a4)	$2.3RT/F$	59	1			Y
		$M\text{-}COOH\text{–}H^+ + e^- \rightarrow M\text{-}CO + H_2O$ (a7)	$2.3RT/F(\alpha-2)$	39	2			N
		$M\text{-}CO \rightarrow CO + M$ (a9)	$2.3RT/2F$	30	2			N
	Type 3	$CO_2 + H_2O + e^- + M \rightarrow M\text{-}COOH + OH^-$ (a3)	$2.3RT/F(\alpha-1)$	118	0			Y
		$M\text{-}COOH + H_2O + e^- \rightarrow M\text{-}CO + H_2O + OH^-$ (a6)	$2.3RT/F(\alpha-2)$	39	1			Y
		$M\text{-}CO \rightarrow CO + M$ (a9)	$2.3RT/2F$	30	2			N
HCO_3^-	Type 4	$CO_2 + e^- + M \rightarrow M\text{-}CO_2^-$ (a1)	$2.3RT/F(\alpha-1)$	118	0	0–1	0	N
		$M\text{-}CO_2^- + HCO_3^- \rightarrow M\text{-}COOH + CO_3^{2-}$ (a2)	$2.3RT/F$	59	1		1	Y
		$M\text{-}COOH + e^- \rightarrow M\text{-}COOH^-$ (a5)	$2.3RT/F(\alpha-2)$	39	1		0	N
		$M\text{-}COOH^- + HCO_3^- \rightarrow M\text{-}CO + H_2O + CO_3^{2-}$ (a8)	$2.3RT/2F$	30	2		1	Y
		$M\text{-}CO \rightarrow CO + M$ (a9)	$2.3RT/2F$	30	2		−2	N
	Type 5	$CO_2 + HCO_3^- + e^- + M \rightarrow M\text{-}COOH + CO_3^{2-}$ (a3)	$2.3RT/F(\alpha-1)$	118	1		1	Y
		$M\text{-}COOH + HCO_3^- \rightarrow M\text{-}COOH\text{–}H^+ + CO_3^{2-}$ (a4)	$2.3RT/F$	59	1		1	Y
		$M\text{-}COOH\text{–}H^+ + e^- \rightarrow M\text{-}CO + H_2O$ (a7)	$2.3RT/F(\alpha-2)$	39	2		0	N
		$M\text{-}CO \rightarrow CO + M$	$2.3RT/2F$	30	2		−2	N
	Type 6	$CO_2 + HCO_3^- + e^- + M \rightarrow M\text{-}COOH + CO_3^{2-}$ (a3)	$2.3RT/F(\alpha-1)$	118	0		1	Y
		$M\text{-}COOH + HCO_3^- + e^- \rightarrow M\text{-}CO + H_2O + CO_3^{2-}$ (a6)	$2.3RT/F(\alpha-2)$	39	1		1	Y
		$M\text{-}CO \rightarrow CO + M$	$2.3RT/2F$	30	2		−2	N
Mixed	Type 7	$CO_2 + HCO_3^- + H_2O + 2e^- \rightarrow CO + OH^- + CO_3^{2-} + H_2O$					0.5	

[a] M: active site; a: assuming $\alpha = 0.5$; $T = 298$ K.

Table 2 Reaction kinetic parameters under the assumption of various rate-determining steps (RDSs) for CH_4 formation during electrocatalytic CO reduction

Proton donor		RDS	Tafel mV dec^{-1} [a]		Reaction order H^+	Reaction order P_{CO}	KIE
H_2O	Type 1	$H_2O + e^- + M \rightarrow M\text{-}H + OH^-$ (c3)	$2.3RT/F(\alpha-1)$	118	0	0–1	Y
		$M\text{-}H + M\text{-}CO \rightarrow M\text{-}CO(H) + M$ (c4)	$2.3RT/F$	59	1		
		$M\text{-}H + M\text{-}CO(H) \rightarrow M\text{-}CO(H)_2 + M$ (c5)	$2.3RT/2F$	30	2		
		$H_2O + e^- + M\text{-}CO \rightarrow M\text{-}CO(H) + OH^-$ (c1)	$2.3RT/F(\alpha-1)$	118	0		
		$H_2O + e^- + M\text{-}CO(H) \rightarrow M\text{-}CO(H)_2 + OH^-$ (c2)	$2.3RT/F(\alpha-2)$	39	1		
H^+	Type 2	$H^+ + e^- + M \rightarrow M\text{-}H$ (c3)	$2.3RT/F(\alpha-1)$	118	1		
		$M\text{-}H + M\text{-}CO \rightarrow M\text{-}CO(H) + M$ (c4)	$2.3RT/F$	59	1		
		$M\text{-}H + M\text{-}CO(H) \rightarrow M\text{-}CO(H)_2 + M$ (c5)	$2.3RT/2F$	30	2		
		$H^+ + e^- + M\text{-}CO \rightarrow M\text{-}CO(H) + OH^-$ (c1)	$2.3RT/F(\alpha-1)$	118	1		
		$H^+ + e^- + M\text{-}CO(H) \rightarrow M\text{-}CO(H)_2 + OH^-$ (c2)	$2.3RT/2F$	30	2		

[a] M: active site; a: assuming $\alpha = 0.5$; $T = 298$ K.

is potentially independent and the symmetry factor is 0.5 or 0 when the RDS involves one electron transfer or not, respectively, the corresponding Tafel slopes were theoretically calculated, as shown in Tables 1–3.

The derivation of electrochemical reaction orders is very complex, particularly for conditions under Langmuir or Temkin isotherm governing the adsorption of electrochemically formed intermediates (*e.g.*, $*CO_2$, *CO, $*CH_x$, *H) in electrocatalytic $CO_{(2)}$ reduction. Recently, Baz *et al.* extended the concept of ''degree of rate control'' ($X_{RC,i}$) to electrochemistry, indicating that the $X_{RC,i}$ in electrochemistry is the weighting factor quantitating the number of electrons transferred to generate each intermediate or product species, which is significantly related to the coverages of intermediates and local microenvironment.[89] Then, the experimentally apparent reaction order with respect to reactant species j (δ_j) is a function of the generalized $X_{RC,i}$, and the corresponding expression is as follows:

$$\delta_j = -\sum_i \left(v_{j\in G^0_{f,i}}\right) X_{RC,i} \quad (6)$$

where $v_{j\in G^0_{f,i}}$ is the stoichiometric coefficient to form intermediate or product species i from reactant j. For further details regarding the degree of rate control, readers are referred to

Table 3 Reaction kinetic parameters under the assumption of various rate-determining steps (RDSs) for C_{2+} formation during electrocatalytic CO reduction

	RDS	Tafel mV dec^{-1} [a]		Reaction order H^+	Reaction order P_{CO}	KIE
Type 1	M-CO + M-CO + e^- → M-$C_2O_2^-$ +M (d1)	$2.3RT/F(\alpha-1)$	118	0	0–2	N
	M-CO + CO(g) + e^- → M-$C_2O_2^-$ +M (d2)	$2.3RT/F(\alpha-1)$	118	0	0–2	N
	H_2O + e^- + M-CO → M-CO(H) + OH^- (d3)	$2.3RT/F(\alpha-1)$	118	0	0–2	Y
Type 2	H^+ + e^- + M → M-H (d3)	$2.3RT/F(\alpha-1)$	118	1	0	Y
	H^+ + e^- + M-CO → M-CO(H) (d4)	$2.3RT/F(\alpha-1)$	118	0	0–2	Y
	M-CO + e^- + M-CO(H) → M-C_2O_2(H)$^-$ (d5)	$2.3RT/F(\alpha-2)$	39	1	0–2	Y
	M-CO(H) + e^- + M-CO(H) → M-C_2O_2 $(H)_2$ $^-$	$2.3RT/F(\alpha-2)$	39	1	0–2	Y
	M-H + M-CO → M-CO(H) +M (d4)	$2.3RT/2F$	59	1	0–1	Y
	M-H +M-CO(H) → M-$CO(H)_2$ + M	$2.3RT/2F$	59	2	0–1	Y

[a] M: active site; a: assuming α = 0.5; T = 298 K.

previous reviews.[90–93] Herein, we just show the range of reaction order values when assuming different RDSs due to the complexity, as shown in Tables 1–3.

Therefore, the RDS can be identified by comparing the experimentally-obtained and theoretically calculated results. However, Tables 1–3 clearly show that different RDSs could give the same Tafel slopes. To provide deeper insight into reaction pathways, the reaction orders with respect to pH, $c_{HCO_3^-}$, and $P_{CO_{(2)}}$ are needed to further support the proposed reaction mechanism. For example, the proton donor type could be distinguished by combining the reaction orders with respect to pH and $c_{HCO_3^-}$. Moreover, the isotopic effect could serve as valuable supplementary information in proposing RDS, where the KIE is not unity if the proton was involved (detailed discussions in next section).

3. Microkinetic analysis of diverse experimental results in electrocatalytic $CO_{(2)}$ reduction

In the past decades, the quantitative measurements of kinetic observables (*e.g.*, Tafel slope and reaction order) were performed in electrocatalytic $CO_{(2)}$ reduction, which was utilized to screen the electrocatalysts and interpret the corresponding reaction pathways. However, great discrepancies often arise in interpreting the experimental kinetic results, related to the complexity of electrocatalytic $CO_{(2)}$ reduction occurring on the electrode. This section systematically reviews the experimentally obtained kinetic observables, the proposed RDSs, and reaction mechanisms over various electrocatalysts in electrocatalytic $CO_{(2)}$ reduction (Tables 4 and 5). The analysis of Tafel slopes and reaction orders will be discussed, and reasonable explanations of the discrepancies in the literature will be analyzed. Later, the discussions were further extended to KIE and temperature-sensitivity analysis. It should be explicitly mentioned that the macroscopic observables in the literature including Tafel slope, reaction order, isotopic effect, and activation energy are ''apparent'', which does not have to reflect the intrinsic kinetics of electrocatalysts. Their values are usually convoluted by non-kinetic effects, electrolyte effects, mass transport, different proton donors, homogeneous reactions, and bubbles. Hence, the macroscopic observables in this review represent the apparent ones unless otherwise specified. More detailed discussions can be found in the following section.

3.1 Summary of Tafel slopes and reaction orders for CO evolution over various electrocatalysts in the literature

3.1.1 Experimentally obtained Tafel slopes of CO evolution. Beginning with the simplest two-electron transfer for CO evolution in electrocatalytic CO_2 reduction, Table 4 summarizes the reaction conditions, kinetic observables, and proposed RDSs over TMs, molecular complexes, and MNC_S. The as-obtained Tafel slopes and reaction orders are rather scattered due to different experimental conditions and nano-structured electrocatalysts. For example, the reported Tafel slopes for CO evolution on Ag and Au clearly showed various values from *ca.* 50 to 140 mV dec^{-1}, yielding different RDSs. Sargent and co-workers examined different nano-structured Au in electrocatalytic CO_2 reduction toward CO using conventional H-type cell and different Tafel slopes of 42 mV dec^{-1}, 80 mV dec^{-1}, and 96 mV dec^{-1} were obtained on Au needles, rods, and particles, respectively (No. 1).[94] The RDS was proposed to change from the first-electron transfer step on Au particles to the second-electron transfer step on Au needles, and the enhancement of electron transfer was ascribed to the sharp-tip enhancement effect.[94]

The Chan group also reported similar results that a lower Tafel slope of close to 59 mV dec^{-1} on oxide-derived Au electrodes was obtained than that of *ca.* 118 mV dec^{-1} on polycrystalline (PC) Au foil, resulting from more stabilization of proposed *CO_2^- intermediate on oxide-derived (OD) Au surface (No. 2).[95] However, the Xu group reported that even bulk PC-Au electrode also could deliver a Tafel slope of *ca.* 59 mV dec^{-1} at sufficiently low overpotentials (>-0.4 V *vs.* RHE), and an obvious transient was observed at -0.4 V *vs.* RHE, ascribed to the mass transport limitations (No. 3).[26] Recently, Chan and co-workers revisited the long-standing controversy surrounding the RDS on Au and developed multi-scale modeling integrating *ab initio* microkinetic kinetics, mass transport simulations, and the effect of charged electric double layer (No. 4) (Fig. 5a).[32] Various experimentally reported Tafel slopes were ascribed to

Table 4 Reported Tafel slopes, reaction orders, and proposed RDSs in electrocatalytic CO_2 reduction to CO over various electrocatalysts at different conditions

No.	Catalyst	Electrolyte	Potential range (V *vs.* RHE)	Tafel mV dec^{-1}	Proton	Reaction orders $c_{HCO_3^-}$	RDS	Ref.
1	Au-needles	0.5 M $KHCO_3$	−0.2 to −0.3	42			a5	94
	Au-rods		−0.3 to −0.5	80			a1	
	Au-particles		−0.3 to −0.5	96			a1	
2	OD-Au	0.5 M $NaHCO_3$	−0.2 to −0.3	56	HCO_3^-	0.96	a2	95
	PC-Au		−0.4 to −0.6	114			a1	
3	Au foil	1.0 M $NaHCO_3$	−0.3 to −0.4	56	HCO_3^-	0.9[c1]	a4	26
	Au foil		−0.4 to −0.43	134			a1	
4	PC-Au	0.1 M $KHCO_3$	> −0.3	42	H_2O	0	a6	32
	PC-Au		< −0.3	101		0	a1	
5	Cl-modified Au	0.2 M $KHCO_3$	−0.3 to −0.5	61			a2	98
	CN-modified Au		−0.35 to −0.5	45			a2	
6	PC-Ag	0.5 M $KHCO_3$	> −0.5 V	67	H_2O	0	a2	26
7	PC-Ag	0.5 M $NaHCO_3$	−0.6 to −0.9	134	H_2O/HCO_3^-	0.5[c2]	a1	31
	Nanoporous Ag		−0.2 to −0.4	58			a4	
	Ag Nanoparticle		−0.3 to −0.5	64			a4	
	PC-Ag	0.1 M $KHCO_3$	> −0.4	51	H_2O	0	a4	97
8			−0.65 < < −0.4	138		0	a1	
			< −0.65	163		0	a1 + LRC	
9	PC-Ag	0.1 M $KHCO_3$	−0.2 to −0.6	157	H_2O	0	a1	99
10	Molecular film@Ag	0.1 M $KHCO_3$	−0.3 to −0.6	91	HCO_3^-	1	a3	
11	Ag_3Au	0.1 M $KHCO_3$	−0.2 to −0.3	48	H_2O	0	a6	100
12	$Au_6Ag_2Cu_2$	0.5 M $KHCO_3$	−0.2 to −0.3	94			a1	101
13	CoPc/CNT	0.1 M $NaHCO_3$	−0.5 to −0.7	118	H_2O	0.17	a1	102
	CoPc/CNT	1 M $NaHCO_3$			HCO_3^-	1.4	a3	
14	CoPc/CNT	1 M $NaHCO_3$	−0.4 to −0.6	120	H_2O	0	a1	34
15	Co-QC	0.1 M $KHCO_3$	−0.2 to −0.35	119	H_2O	0	a1	103
16	Ni-TAPc	0.5 M $KHCO_3$	−0.4 to −0.6	72	HCO_3^-	0.8	a2	104
17	ZrO_2@NiNC	0.5 M $KHCO_3$	−0.4 to −0.5	72	H_2O		a2	105
18	Ni–N–C	0.5 M $KHCO_3$	−0.5 to −0.6	132		0	a1	106
	Ni–N_3-NCNFs		−0.3 to −0.6	71			a2	
19	Sn doped Cu	0.1 M $KHCO_3$	−0.3 to −0.5	109	HCO_3^-	1	a3	107
		0.3 M $KHCO_3$		112				
		0.7 M $KHCO_3$		116				
20	PC Sn	1 M $NaHCO_3$	−0.5 to −0.8	116			b1	108
21	In_2S_3	0.5 M $KHCO_3$	−0.6 to −0.7	233	H_2O		b1	109
	$AgIn_5S_8$			77.4			b2	
	$AgInS_2$			74			b2	

Note PC: polycrystalline; CoQC: cobalt quaterpyridine complexes; Ni–N_3-NCNFs: N atoms and coordinatively unsaturated Ni–N_3 moieties co-anchored carbon nanofiber; c1: electrolyte 0.04–0.1 M $NaHCO_3$ for reaction order of HCO_3^-; c2: electrolyte 0.1–1.0 M $NaHCO_3$ for reaction order of HCO_3^-; LRC: local reaction environment control.

Table 5 Summary of experimentally kinetic observables over Cu-based electrocatalysts in electrochemical CO reduction to C_{2+} products

			Kinetic order to P_{CO}					pH dependence	Tafel	
No.	Cell	P_{CO}(kPa)	C_{2+}	C_2H_4	C_2H_5OH	Acetate	*n*-PrOH	C_{2+}	mV dec^{-1}	Ref.
22	H-Cell									57
23	H-Cell	<50	2	1	0			No	118	134
		≥50	2	2	0					
24	H-Cell	<60	Positive	Positive	Positive	Positive	Positive		118	135,136
		≥60	0	0	0	0	0			
25	H-Cell	<60	Positive	1	Positive	Positive	Positive		118	137
		≥60	0	0	0	0	0			
27	GDE $Cu_{70}Pd_{30}$	<63				0.5			118	138
		≥63				0			118	
	GDE[2] $Cu_{49}Pd_{51}$	<25				1			124	
		≥25				0				
	H-cell[a]	>1010	0.82	0.5	0.87					139
28	GDE	≥30				0.58			118	140
		<30				0.86				
29	GDE	<20.2	1.1	1.1	1.1	0.6 ± 0.2	0.7 ± 0.2		120	
		≥20.2	0	−0.2	−0.3	0.6 ± 0.3	0.7 ± 0.3			

Note: Cu-based GDE was examined in a gas-fed flow cell [a] High-pressure H-type cell.

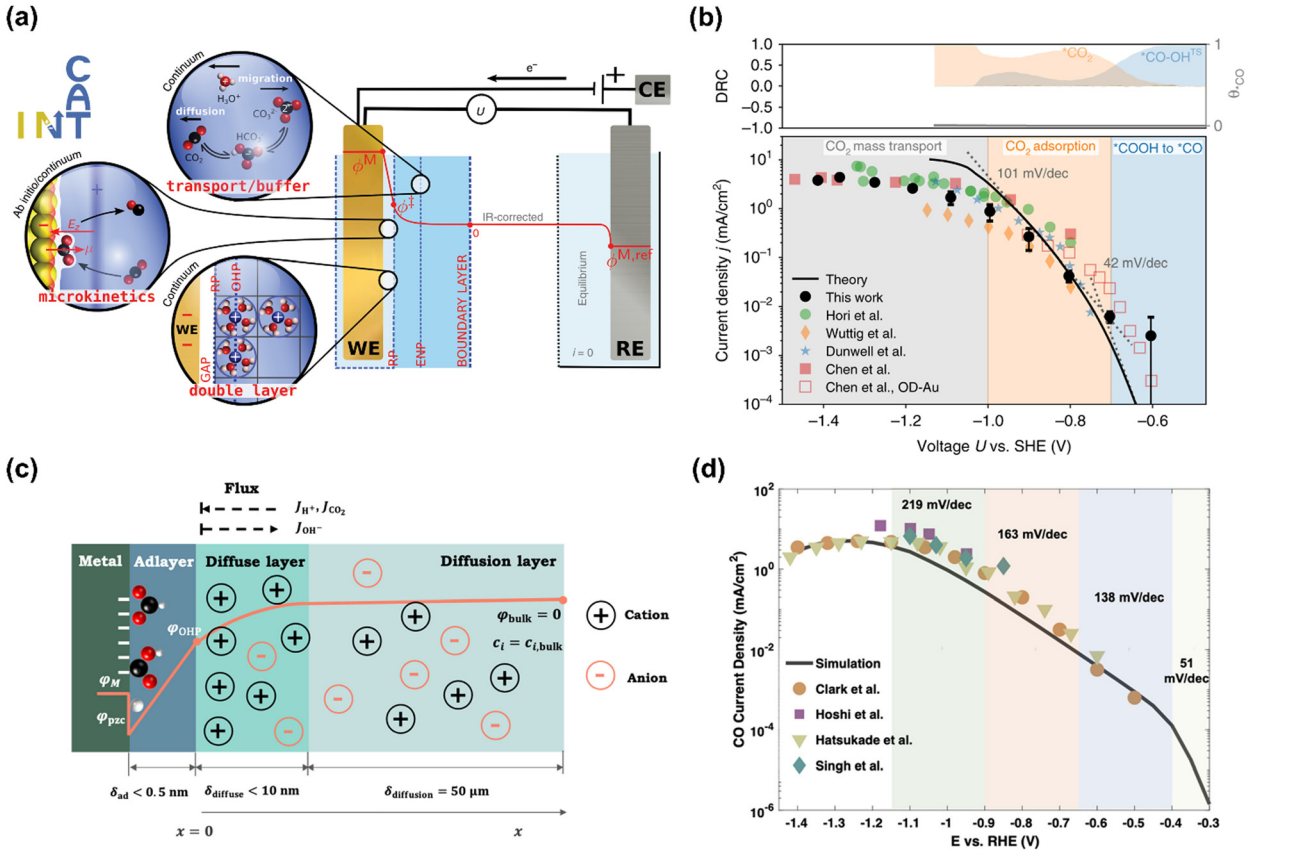

Fig. 5 (a) Schematic illustration of the multi-scale system. (b) Multi-scale CO_2 electroreduction simulation results over Au compared with experiments. Reproduced with permission.[32] Copyright 2020, Nature publishing group. (c) Schematic illustration of the model system. (d) Multi-scale CO_2 electroreduction simulation results over Ag compared with experiments. Reproduced with permission.[97] Copyright 2021, American Chemical Society.

the adsorption of CO_2 modulated by the potential dependence of the surface-charge density and the corresponding electric double-layer field, where CO evolution was separately limited by the conversion of *COOH to *CO at very low overpotentials, CO_2 adsorption induced by the double-layer charging at higher overpotentials, and then CO_2 transportation limitation at <-1.0 V *vs.* SHE, in agreement with the findings in the literature (Fig. 5b).[33,35,95,96]

Similarly, various Tafel slopes were reported over Ag-based electrocatalysts in the literature (No. 6–10) (Table 4). Zhu *et al.* developed a hierarchical model including intrinsic reaction kinetics, specific surface charging state at a given electrode potential, and mass transport effects to elucidate the reaction mechanism and kinetics of CO_2 electroreduction to CO on Ag electrode (No. 8) (Fig. 5c).[97] This study highlighted that the local reaction environment could significantly affect the experimental results and perturb the reaction mechanism. The scattered Tafel slopes in the literature were explained to be affected by the surface charging relation and mass transport effects (Fig. 5d). In addition, several reasons were proposed to decrease the reaction rate of CO evolution at high overpotentials, including the decreased CO_2 concentration, increased pH, surface charge effects, and lateral interactions between *HCOO, *COOH, and *H. This model well explained the reported Tafel slopes in other studies.[110–113] It is worth noting that rigorous analysis of the catalytic activity normalized to the electrochemical surface area (ECSA) likely suggested that nanostructuring does not significantly alter the intrinsic activity of the active sites.[114] The as-obtained kinetic observables and reaction rates varied in the literature since they were affected not only by the intrinsic kinetics but also by the local reaction environments.

Additionally, the reaction rate of electrochemical CO_2 reduction is significantly affected by the adsorption energies of reaction intermediates,[115] which are typically correlated through thermodynamic scaling relations.[116] Strategies to break linear scaling relations and regulate reaction pathways are highly desired to tune the activity and selectivity,[117–119] for example, introducing additive modifications to electrode surfaces (*e.g.*, molecular complexes or anion species) and alloying multi-metallic electrocatalysts.[101,120–125] For example, the Tafel slopes of CN and Cl modified Au electrodes in electrocatalytic CO_2 reduction to CO were 45 and 61 mV dec^{-1}, respectively, lower than that of bare Au (*ca.* 120 mV dec^{-1}), indicating the shifted RDSs in the presence of adsorbed anion (No. 5).[98] Peters and co-workers introduced pyridinium-based additives on the PC-Ag surface, which exhibited a lower Tafel slope of 91 mV dec^{-1} than that of bare PC-Ag, likely due to the suppression of proton but not CO_2 mass transport in electrochemical

CO evolution (No. 10).[99] A similar improvement was reported over ethylenediamine tetramethylenephosphonic acid (EDTMPA) modified Pc-Cu for electrocatalytic CO_2 reduction to CH_4, where a reduced Tafel slope from 144 to 87 mV dec^{-1} in the presence of EDTMPA was observed. Breaking linear scaling relations between the two coupled intermediates (*CO and *CHO) was confirmed by Tafel analysis and theoretical calculation of binding energy and free energy change, thus improving the kinetics of CH_4 formation.[126] In addition, the changed Tafel slopes over alloy electrocatalysts were also demonstrated on Ag and Au-based alloys in electrocatalytic CO_2 reduction to CO (No. 11 and No. 12).[100,101]

For molecular complexes and atomically dispersed electrocatalysts (MNCs), the Tafel analysis is also widely utilized to elucidate their RDSs in electrocatalytic CO_2 reduction. For example, the heterogenized CoPc or CoTPP delivered a Tafel slope of 120 mV dec^{-1} at low overpotential, indicating a slow first electron transfer as the RDS in electrocatalytic CO_2 reduction to CO (No. 13 and 14).[34,102,127–129] Then, pyridine-functionalized cobalt complexes on a carbon substrate could reduce the Gibbs free energy of CO_2 activation further than its counterpart ones and exhibited smaller Tafel slopes, facilitating charge transfer and increasing the activity of CO evolution (No. 15).[103] Moreover, Zheng *et al.* reported that the electronegative N atoms and coordinatively unsaturated Ni–N_3 moieties co-anchored carbon nanofiber (Ni–N_3-NCNFs) catalyst exhibited the positive effect on facilitating CO_2 adsorption and H_2O dissociation steps, thus accelerating the reaction kinetics with a lower Tafel slope of 71 mV dec^{-1} (No. 18).[106] The presence of ZrO_2 next to the atomically dispersed Ni–N_4 sites also could accelerate H_2O activation, resulting in a lower Tafel slope (*ca.* 72 mV dec^{-1}) (No. 17).[105]

It is worth noting that since the Tafel slope is not sensitive to the variance of the proton donor type, the interpretation of RDS and reaction mechanism still needs more evidence, like other kinetic parameters, operando spectroscopies, or theoretical calculations.

3.1.2 Experimentally obtained reaction orders for CO_2 electroreduction. Beyond the Tafel slope, determining reaction orders is an important part of the microkinetic analysis concerning mechanistic interpretation. Especially, reaction order with respect to pH and $c_{HCO_3^-}$ (x) could distinguish a coupled or decoupled elementary proton-electron transfer mechanism in electrocatalytic CO_2 reduction. However, in Table 4, various reaction orders with respect to $c_{HCO_3^-}$ on the same electrolyte could be observed, which leads to different conclusions on the RDS and the roles of bicarbonate. For example, x = 0,[97,130] 0.4,[97] and 0.5[31,33] were reported on PC-Ag; x = 0,[26] and 1[33,95] were obtained on PC-Au and Au nanoparticle, respectively; x = 0,[34] 0.1,[102] and 0.6[102] were delivered on CoPc/CNT. These studies lack agreement regarding the bicarbonate order dependence, impeding the rational catalyst design.

The obvious discrepancies largely arise from the different local reaction microenvironments and misleading interpretations. It is worth noting that the HCO_3^- can be involved in homogeneous reactions *via* eqn (7) and (8) under electrochemical reaction conditions.

$$CO_2 + OH^- \rightleftarrows HCO_3^- \quad (7)$$

$$HCO_3^- + OH^- \rightleftarrows CO_3^{2-} + H_2O \quad (8)$$

Hence, the local reaction microenvironments at the electrode surface change when varying $c_{HCO_3^-}$, including local pH and cation concentration. The cation identity and concentration have been demonstrated to significantly impact on the catalytic performance of electrocatalytic CO_2 reduction due to the interfacial electric and nonelectric field components.[131–133] Moreover, the changed local pH will lead to different values of as-obtained reaction order with respect to $c_{HCO_3^-}$ on SHE and RHE scales. More specifically, the applied potential in RHE changes since the local concentration of c_{H^+} varies and their relationship is applied to the Nernst eqn (9).

$$\Delta E_{RHE} = \Delta E_{SHE} - \frac{2.3RT}{F} \log c_{H^+} \quad (9)$$

For example, when $c_{HCO_3^-}$ is increased from 0.1 M to 1.0 M at fixed ionic strength, the solution pH will shift from 6.8 to 7.7 and the corresponding driving force will increase by *ca.* 59 mV when neglecting the surface charging effect. Eikerling and co-workers rigorously investigated the dependence of $c_{HCO_3^-}$ on PC-Ag in electrocatalytic CO_2 reduction to CO, and the same ionic strength of electrolytes containing different $c_{HCO_3^-}$ was prepared by changing the ratio of $KHCO_3$ and $KClO_4$.[97] The j_{CO} was found to remain constant with varied $c_{HCO_3^-}$ irrespective of overpotential on SHE scale, as shown in Fig. 6a. However, the rate was sensitive to $c_{HCO_3^-}$, exhibiting positive orders (*ca.* 0.4) on $c_{HCO_3^-}$ at −0.7, −0.8, and −0.9 V *vs.* RHE (Fig. 6b), in agreement with the theoretical value (0.5), indicating HCO_3^- was involved in CO_2 reduction as proton source. These results revealed that misleading interpretations could yield contradictory conclusions even when rigorously performed experiments.

In contrast to low overpotentials, the concentration of bicarbonate varied the CO evolution rate at higher overpotentials. In Fig. 6c, the j_{CO} increased as $c_{HCO_3^-}$ increased with a positive slope on an even SHE scale and the slope was larger when the overpotential was higher in the presence of mass transportation limitation. This enhancement was ascribed to bicarbonate contributions as buffer species to maintain the local pH and suppress the eqn (7) to consequently enhance the local CO_2 concentration, as shown in Fig. 6d.[97] Consistently, electrocatalytic CO_2 reduction over Co complexes exhibited positive and zeroth orders kinetics on bicarbonate on SHE scale in H-cell[102] and gas-fed flow cell (irrespective of overpotential),[34] respectively, where mass-transfer limitation was circumvented due to the construction of three-phase interface in gas-fed flow cell under reaction conditions.

Following up on this point, the differences in the local reaction environment can explain the contradicting results of bicarbonate order dependence in the literature. For example, the reported bicarbonate dependences on PC-Ag were 0, and 0.5

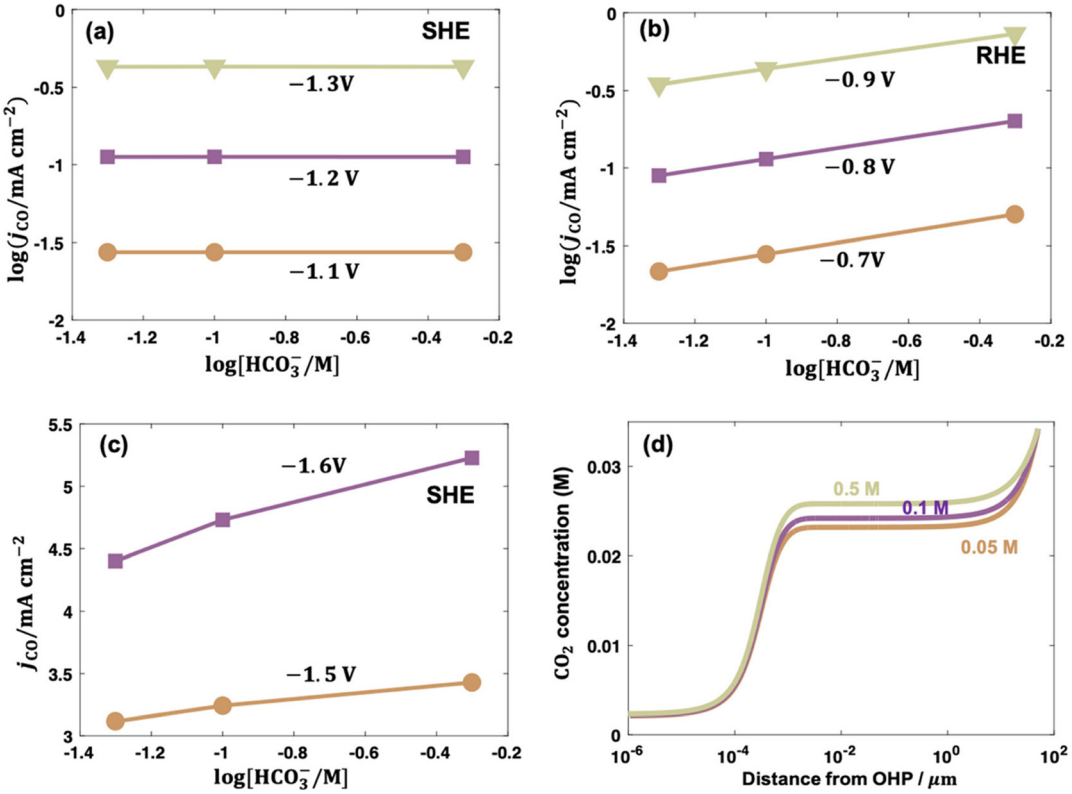

Fig. 6 Bicarbonate order dependence of electrocatalytic CO_2 reduction to CO over PC-Ag under fixed ionic strength and at (a) −1.1, −1.2, −1.3 V *vs.* SHE; (b) at −0.7, −0.8, −0.9 V *vs.* RHE; and (c) at −1.5 and −1.6 V *vs.* SHE. (d) Concentration distributions of CO_2 in solutions with 0.05, 0.1, and 0.5 M bicarbonate at −1.6 V *vs.* SHE. Reproduced with permission.[97] Copyright 2021, American Chemical Society.

in different studies, which were caused by using different potential scales. The first-order dependence on PC Au and Au nanoparticles likely resulted from the combined effects of different potential scales and mass transportation effects. It also should be noted that phosphate was selected to maintain the ionic strength, which may lead to specific adsorption of buffering anions to poison the CO evolution on PC-Au and promote the H_2 evolution.[33,130] Additionally, some abnormal values appeared when the experiments were conducted in electrolytes containing different $c_{HCO_3^-}$ with different ionic strength.[102,107]

3.2 Tafel and reaction order analysis of electrocatalytic CO reduction over Cu

As described in Section 2, CO is a key and necessary intermediate during electrocatalytic CO_2 reduction to CH_4 and C_{2+} compounds.[57,141] Moreover, CO can alleviate the complexity of the multiple equilibrium reactions between CO_2 and aqueous electrolytes. Hence, the development of microkinetic analysis of electrochemical CO reduction has attracted tremendous attention in recent years, which can be extended to the rational design of efficient catalysts in electrocatalytic CO_2 reduction. This section reviews the studies on the Tafel and reaction order analysis for electrochemical CO reduction to C_{2+} and CH_4 formation, focusing on the reaction order with respect to P_{CO} (Table 5), where significant effects of reactor configuration on the reaction order measurements will be discussed.

A pioneering work was reported by Hori *et al.* in 1997, which demonstrated the efficient electrochemical CO reduction to CH_4 and C_{2+} on Cu in a H-type Cell and disclosed their molecular-level reaction pathways with regard to microkinetic analysis (No. 22). Their study revealed that the reaction rates of C_2H_4 and C_2H_5OH were insensitive to pH of electrolyte, where H_2O as the proton source for C_2H_4 and C_2H_5OH formation was proposed. In contrast to C_2H_4 and C_2H_5OH formation, the reaction rate of CH_4 was proportional to proton activity and followed the Tafel relationship. However, their Tafel slopes were abnormal (>118 mV dec^{-1}), likely arising from the mass transportation limitation. The different transfer coefficients (0.35 for C_2H_4 and 1.33 for CH_4) indicated the reaction paths of CH_4 and C_2H_4 formations were separated at an early stage of CO reduction.[57] Then, Lu and co-workers examined the rigorous electrokinetic analysis by employing a PTFE modified electrode to reduce the CO mass transport limitation in electrocatalytic CO reduction (No. 24 and 25). Based on the measured Tafel slopes (118 mV dec^{-1} for both C_{2+} and each product) and reaction orders with respect to P_{CO} (first-order dependence for C_{2+} products) at P_{CO} < 60 kPa, they proposed that the formation rates of C_{2+} products are most likely limited by the hydrogenation of CO with adsorbed water in H-cell.[135–137] Moreover, the microkinetic analysis by integrating pH-dependent CH_4 formation rate, shifted Tafel slopes at different electrolytes with varied pH, and reaction orders with respect to P_{CO} suggested

that the reaction rate of CH_4 was limited by the CO hydrogenation step *via* a PCET in weakly alkaline electrolytes (*e.g.*, 7 < pH < 11) and a chemical hydrogenation step of CO by adsorbed hydrogen atom at pH > 11, respectively.[135,136] Additionally, Schreier *et al.* investigated the dynamics of CO on the Cu surface, providing deeper insight into the mechanism for the production of H_2, CH_4, and C_2H_4. It should be noted that these experiments were performed at low temperatures in an ethanol medium (−35 °C) to increase CO solubility and surface-affinity. Those findings showed that the reaction rate of C_2H_4 was insensitive to P_{CO}, concluding that C_2H_4 was likely formed *via* *CO dimerization on a *CO saturated surface; the reaction rate of CH_4 was suppressed by increasing P_{CO}, which was interpreted by the competition between *H and *CO on Cu surface to govern the product distributions.[142]

Recently, Kastlunger *et al.* experimentally performed the rigorous Tafel analysis at a wide range of pH values (3–13) in conjunction with constant-potential DFT kinetics to analyze the RDS in CO electroreduction on Cu. Their measured current densities were in agreement with the literature data, as shown in Fig. 7.[86] The as-obtained partial current densities of C_{2+} products at pH 3 exhibited slightly decreased due to the specific adsorption of buffering anions (Fig. 7a), which could block active sites and/or compete with CH_4 and H_2 production.[143] The experimentally obtained Tafel slopes of C_{2+} (Fig. 7a) were consistent with the theoretically derived slopes assuming *CO dimerization as the RDS, where the potential response was considered. Contrary to C_{2+} formation, the partial current densities of CH_4 exhibited pH-dependent activity and did not overlap for these three pH values on the SHE scale, suggesting that the proton donor was different. By analyzing Tafel slopes (*ca.* 40–90 mV dec^{-1}), at lower pH values of 3 and 7, the first PCET step was proposed as the RDS for CH_4 formation; at pH = 13, and the second PCET step was identified as RDS, consistent with Hori's results.[54,57]

Notwithstanding the conflicting results provided by microkinetic analysis, some proposed RDSs can be excluded easily. For example, the hydrogenation of *CO with H_2O[136] cannot be the RDS for C_{2+} formation since the $j_{C_{2+}}$ were undoubtedly demonstrated to be insensitive to pH at ambient pressure and temperature. Only the Tafel slope of 118 mV dec^{-1} and the first reaction order with respect to P_{CO} could not yield exclusive RDS in CO electroreduction. For CH_4 formation, the findings in ethanol media at low temperatures could not be extended to the aqueous conditions at room temperature, where a negligible *H coverage is expected on Cu since H_2 evolution on Cu[142] is limited by the Volmer step. In this context, the competition between *H and *CO over Cu for CH_4 production seems unlikely in aqueous conditions. Moreover, the chemical hydrogenation step of *CO by *H on Cu at (pH > 11) was also proposed as RDS.[136] If so, the current–voltage relationship should overlap on the RHE scale, inconsistent with the experimental results.[86] Indeed, a significant influence of the local reaction environment has been emphasized for the catalytic performance evaluation of $CO_{(2)}$ electroreduction.[144] The activity and selectivity of electrocatalysts change significantly as a function of reaction rate due to local pH and $CO_{(2)}$ availability. It should be noted that all these studies were performed using a conventional aqueous H-cell, which fails to achieve an industrially relevant reaction rate because of the mass-transport limitations. Consequently, the proposed reaction mechanism may be interpreted wrongly due to the operating conditions.

Accordingly, performing a microkinetic assessment in a cell configuration with improved mass transfer flux is essential to understand and design an electrocatalyst. In recent work, an in-depth microkinetic investigation assessed under commercially relevant conditions was performed over Cu using a gas-fed flow cell.[145] Consistently, the reaction rates of C_{2+} products (*e.g.*, C_2H_4, C_2H_5OH, and n-PrOH) over Cu exhibited zeroth orders kinetics on H^+ and OH^- irrespective of P_{CO} and reactor configuration, indicated that water was used as the proton donor.[57,134–136,142] Regarding the effect of P_{CO}, $j_{C_{2+}}$

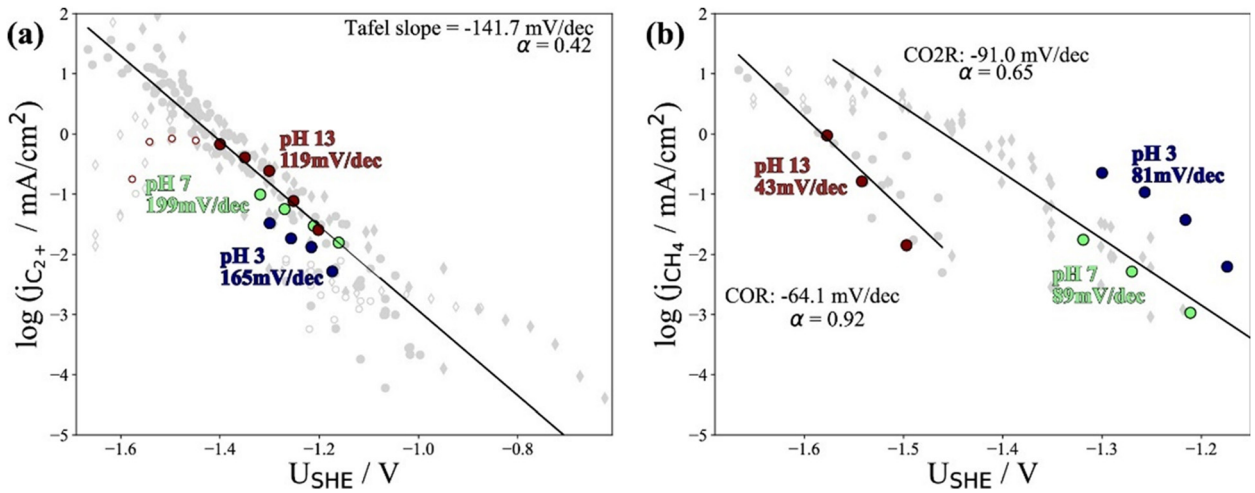

Fig. 7 The partial current densities of (a) C_{2+} products and (b) methane at pH 3, 7, and 13 on PC–Cu foil. Reproduced with permission.[86] Copyright 2022, American Chemical Society.

increased with increased P_{CO} below about 20.2 kPa with a slope of about 1, while above this partial threshold pressure, the rate remained unchanged, indicating that the formation of C_{2+} products shared some early intermediates. Moreover, this overall $j_{C_{2+}}$–P_{CO} relationship was deconvoluted to each product, showing that higher P_{CO} favored *n*-PrOH and acetate at the expense of C_2H_4 and C_2H_5OH. This transition in the reaction orders was not observed in previous studies employing H-cells,[57,134–136,142] most likely due to the distinct local reaction environment. The opposite P_{CO}-dependent trends for different C_{2+} products suggest that the plausible scenario was a shared RDS for all C_{2+} products. Meanwhile the selectivity-determining steps would result in various apparent reaction orders for different C_{2+} products. Overall, the electrokinetic results integrating the Tafel slope (*ca.* 120 mV dec^{-1}), reaction orders concerning pH and P_{CO}, and other kinetic observables suggested that the formation of C_{2+} was likely limited by the formation of M-CO(H)-CO^- species with the surface site predominantly comprising M-CO(H) and the product distribution was perturbed by coverage of *CO as a key intermediate at selectivity-controlling steps after the RDS.[145]

Regarding the local reaction microenvironment created in different reactor configurations, four aspects must be considered. First, the CO availability on Cu is significantly different in conventional H-type cell and GDE-based electrolyzers. In a H-type cell, CO is supplied to Cu surface that was fully or partially immersed in a liquid electrolyte, while CO could be provided *via* the gas-phase using a gas-diffusion layer where a gas–liquid–solid interface is constructed. There is a roughly 3-order of magnitude reduction in CO diffusion pathways to the surface of the catalyst: from *ca.* 50 μm (H-cell) to 50 nm (GDE), resulting in different CO coverage.[144] It was reported that the surface coverage of CO on Cu affected the binding energy of CO and reaction intermediates due to adsorbate–adsorbate interactions, especially under higher coverages.[146,147] For the chemisorption of CO on Cu(111) at low temperatures, the initial heat of adsorption of 50 kJ mol^{-1} was maintained up to one-third coverage and then dropped abruptly to 38 kJ mol^{-1}.[147,148] Second, local pH near the Cu surface varies significantly at low current density and industrially relevant conditions. Although the overall reaction rate of CO electroreduction showed less dependence on pH, it could result in altered energetics of reaction intermediates or reaction pathways as a function of current density. For example, the partial current density for acetate experienced a significant enhancement at elevated OH^- concentration during CO electroreduction.[149,150] It was also reported that local pH affected the adsorption configuration of reactants and intermediates (*e.g.*, flat or vertical mode), resulting in different product distributions in electrocatalytic system.[151,152] Third, the influence of the potential dependence on the reaction energetics, intermediate adsorption, and reaction pathways should be taken into account. The applied potentials can change the binding enthalpy and entropy of reaction intermediate through electric field effects (*e.g.*, the surface dipole moment or polarizability).[153] For example, the previous study revealed that the RDS on gold was *COOH to *CO at low overpotentials and CO_2 adsorption at intermediate overpotentials.[32] Finally, it should be noted that the solvation effect (*e.g.*, hydrogen bond) and bubble formation could also affect the reaction rates and reaction intermediates.[148,154–156] For example, the *COH intermediate could also be stabilized *via* hydrogen bonding between its OH functional group and a neighboring *CO adsorbate.[37]

3.3 KIE study in electrochemical $CO_{(2)}$ reduction

The quantification of KIE can provide deeper insight into whether isotopes are involved in the RDS in heterogeneous catalysis (Fig. 8a and b).[157] Generally, the elementary steps for electrochemical $CO_{(2)}$ reduction fall into one of the following categories: (1) chemical step, (2) ET, (3) CPET, and (4) PT. When the RDS is CPET, PT, or chemical steps with H-containing species, the presence of isotopes in the electrolyte will vary the reaction rate of electrochemical $CO_{(2)}$ reduction. More specifically, KIE is usually categorized into primary KIE, secondary KIE (Fig. 8c), and inverse KIE (Fig. 8d). The cleavage of bonds containing isotopes causes primary KIE, and its magnitude is related to the difference in zero-point energy (ZPE) between the C–H and C–D bonds (Fig. 8a). The maximum KIE is predicted to be 6.5 when the target bond is 100% split at the transition state. Some experimentally obtained KIEs are lower than 6.5 due to the incomplete cleavage of the target bond or the residual ZPE difference between C–H and C–D bonds at the transition state (Fig. 8b).[158–162] Secondary KIE indicates a change in bond hybridizations (*e.g.*, from a sp^3 hybridized C atom to a sp^2 hybridized C atom) rather than bond cleavage, resulting in a maximum value of approximately 1.41 (Fig. 8c).[163,164] On the other hand, a reverse secondary KIE (Fig. 8d) could occur, delivering a maximum value of approximately 0.7 when the C–H bond shows a larger activation energy and a slower reaction rate than the C–D bond.

3.3.1 KIE study on inorganic electrocatalysts in electrochemical $CO_{(2)}$ reduction. KIE analysis is widely utilized as a complementary tool to identify the RDS and key intermediates in electrocatalytic $CO_{(2)}$ reduction. To understand the formation of C_1 products (*e.g.*, CO and HCOOH), Deng *et al.* examined the KIE with respect to the reaction rate of electrochemical CO_2 reduction over TMs and p-block metals in H-type cell.[165] The j_{CO} (Au and Ag) and j_{HCOO^-} (Sn and In) remained identical using D_2O instead of H_2O in the 0.1 M K based-electrolyte, indicating PT or CPET step was not involved in RDS. As expected, HER rates were more severely suppressed by replacing H_2O with D_2O, in agreement with the previous results.[166] In conjunction with the results of pH dependency studies and Tafel slopes, they concluded that the adsorption of CO_2 coupled with one electron transfer was the RDS in electrochemical CO_2 reduction. Consistently, Wuttig *et al.* also observed that j_{CO} over Au exhibited zeroth order dependence on the ratio of hydrogen/deuterium (H/D) ratio under identical conditions.[35] However, the inverse KIE was also obtained on Au foil at a kinetically controlled potential of −0.4 V *vs.* RHE in H-type cell, likely resulting from the convoluting factors (*e.g.*, CO_2 solubility) and competing reaction (HER).[26] For example,

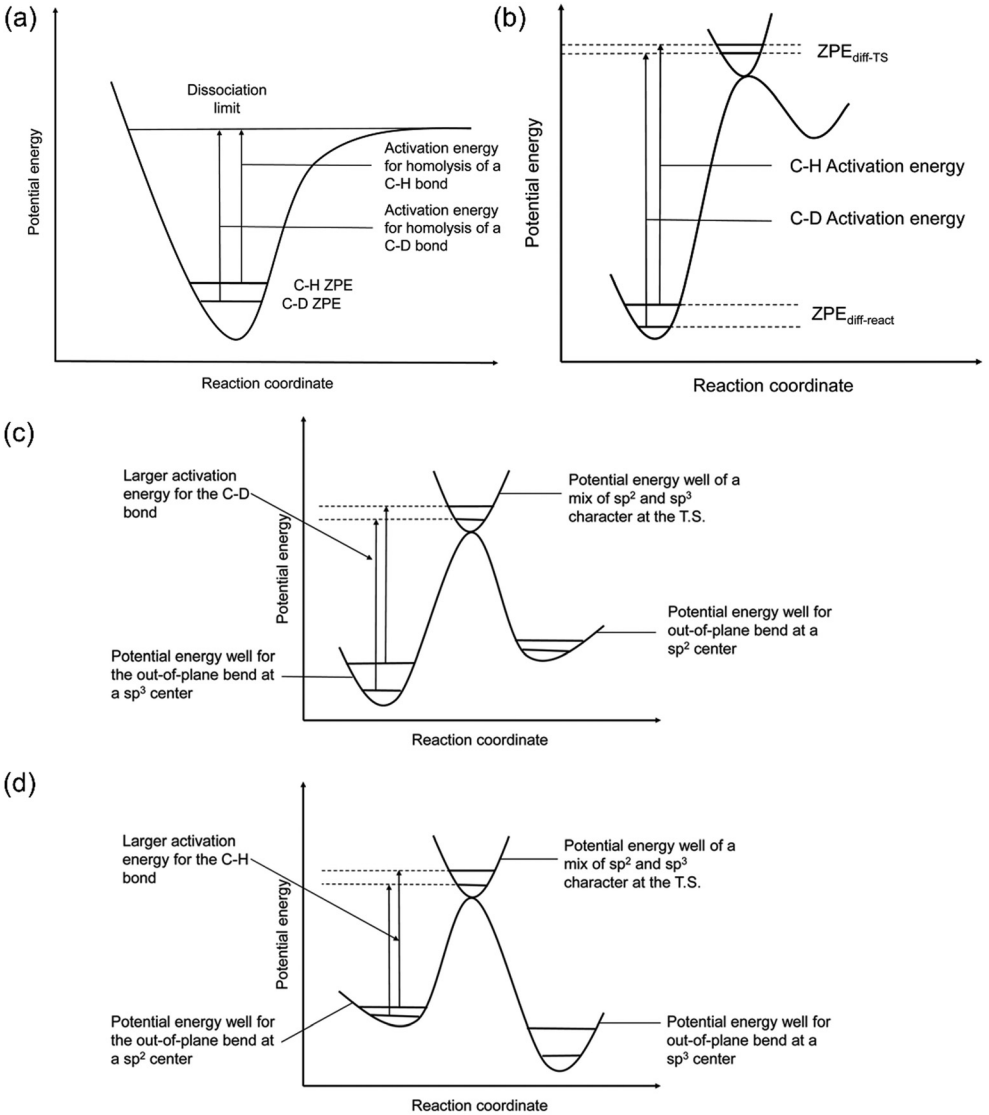

Fig. 8 (a) A scheme of KIE in C–H bond activation. (b) A scheme showing the observed KIE related to the residual ZPE. Energy diagrams showing the (c) normal and (d) inverse secondary KIEs. Reproduced with permission.[157] Copyright 2020, RSC publication.

CO_2 solubility is changed from 33.8 mM in H_2O to 38.1 mM in D_2O.[167] The local microenvironment is again highlighted as perturbing KIE measurements. To avoid the limitation of CO_2 transportation, Verma *et al.* performed KIE studies of CO evolution over Au in a gas-fed flow cell using the 2.0 M NaOD as a catholyte. The nearly identical j_{CO} was observed in both the protonated and deuterated electrolytes, suggesting that H_2O was not involved in RDS over Au, consistent with those obtained in conventional H-type cell.[64]

In conjunction with the deuterium labeling method, isotope measurements could provide more evidence of the reaction mechanism. For example, Ma *et al.* examined the isotopic effects over sulfur-doped In catalyst using H-type cell in electrocatalytic CO_2 reduction to formate. j_{HCOO^-} in K_2SO_4/H_2O was larger than that in the K_2SO_4/D_2O system and the corresponding KIE was around 1.9, consistent with the primary KIE.[168] Additionally, almost 98% of the produced formate was in the form of $DCOO^-$ when D_2O was used to replace H_2O in 0.5 M $KHCO_3$ electrolyte, suggesting the origin of H in formate coming from H_2O rather than HCO_3^-. Taken together, these findings revealed that the dissociation of H_2O was involved in the RDS for electrochemical CO_2 reduction to formate over sulfur-doped In catalyst.[169]

In electrochemical CO reduction to C_{2+}, Chang *et al.* performed isotopic effects on PC–Cu in H-type cell. $j_{C_2H_4}$ was reduced by a factor of *ca.* 3.5 by switching the electrolyte from 1.0 M $NaOH/H_2O$ to 1.0 M $NaOH/D_2O$, consistent with a primary KIE, concluding that H transfer was involved in the RDS for C_2H_4 formation.[137] However, Lu *et al.* carried out similar KIE studies on Cu using a gas-fed flow cell and found that j_{C2H4} in KOH/H_2O was indeed larger than that in the KOD/D_2O system across the potential window. However the apparent KIE was only around 1.2–1.4, likely consistent with a secondary KIE, indicating a change in bond hybridizations

rather than bond formation or cleavage. These results indicate that the decrease in the vibrational frequency after the bond-hybridization for a C–H bond was more significant than that for a C–D bond, leading to smaller activation energy and a faster reaction rate of C_2H_4 formation. The determined KIE (*ca.* 5–7) for HER perfectly agree with the literature data, giving audiences confidence in the accurate KIE of C_2H_4 being measured.[137] The difference between as-obtained KIE in the H-type and gas-fed flow cells likely resulted from the local reaction conditions. These finding could not exclude the RDS involved in hydrogen-containing species (*e.g.*, *CO(H)). More evidence from spectroscopic studies and theoretical calculations is needed to interpret the detailed reaction pathways for CO electroreduction.

Isotopic effects have been widely utilized not only in mechanistic studies, but also in the ration design of catalysts. Wang and co-workers studied the isotopic effect on electrocatalytic CO_2 reduction to C_2H_4 over nano-structured Cu using a gas-fed flow cell. The formation rate of C_2H_4 was suppressed by the replacement of H_2O with D_2O in 1 M KOH electrolyte, and an apparent KIE of up to *ca.* 2 was obtained, indicating that the dissociation of H_2O was involved in the rate-determining step. Interestingly, halogen (I, Br, Cl, and F)-modified copper catalysts resulted in the decreased KIE, delivering values of 1.8, 1.5, 1.3 and 1.2 over I–Cu, Br–Cu, Cl–Cu and F–Cu catalysts, respectively. The KIE over the F–Cu catalyst close to 1 indicated that the presence of F on copper accelerated H_2O activation, which was no longer the rate-determining step over this catalyst.[170] Moreover, Guo *et al.* observed a primary KIE (*ca.* 2.9) in electrocatalytic CO_2 reduction to CO over layered bismuth subcarbonate ($Bi_2O_2CO_3$; BOC) in a gas-fed flow cell, which indicated that the O–H cleavage of water was involved in the RDS. When Ag was introduced to adjacent Bi sites (Ag/BOC), the corresponding KIE was decreased to *ca.* 2.5, suggesting that Ag could accelerate the dissociation of H_2O to supply reactive hydrogen species to facilitate CO_2 hydrogenation to produce formate.[171]

3.3.2 KIE study on molecular complexes in electrochemical CO_2 reduction. Apart from inorganic electrocatalysts, KIE analysis is also a powerful tool to identify the RDS and key intermediates for molecular complexes in homogeneous and heterogeneous CO_2 electroreduction. For example, Dey *et al.* examined the isotopic effects on cobalt pyridine thiolate complexes in homogeneous CO_2 electroreduction to formate and reported a primary KIE of 8.2, indicating that the RDS involved a proton transfer and provided indirect evidence on the formation of Co-H species.[172] Khadhraoi *et al.* collected isotopic effects on a series of tetra-, di- and mono-substituted iron porphyrins with cationic imidazolium functions (named as 4-im-Fe, 2-im-Fe, and 1-im-Fe) in homogeneous CO_2 electroreduction to CO.[173] KIE was measured for each imidazolium derivative using H_2O or D_2O as a proton or deuterium source, exhibiting a strong inverse KIE of 0.43 over 4-im-Fe and unity KIE over 2-im-Fe (1.1) and 1-im-Fe (1). The inverse KIE over 4-im-Fe indicated a pre-equilibrium step preceding the rate-determining protonation significantly contributed to the overall kinetic of CO_2 electroreduction, likely resulting from the H_2O molecular nanoconfinement, which was reported in various ionic liquids, including those based on imidazolium groups.[174–176] These findings suggested that through-structure inductive effects and through-space electrostatic interactions could induce the change of RDS in iron porphyrins during CO_2 electroreduction. Similarly, Tignor *et al.* investigated the isotopic effects over various manganese electrocatalysts bearing pendant H-bond donors at different positions in CO_2 electroreduction to CO. Isotope effects associated with CO_2 electroreduction were observed over electrocatalysts substituted bipyridine ligands with phenol and anisole at the 4-and 6-positions, indicating that intramolecularly hydrogen bond perturbed both the reactive intermediates and the transition state associated with cleavage of the carbon dioxide C–O bond.[177]

For heterogeneous molecular catalysts, McCrory and co-workers conducted KIE studies to investigate the influence of axial ligand coordination on CoPc during electrocatalytic CO_2 reduction in H-type cells. The parent CoPc exhibited identical KIE in H-based and D-based electrolytes, which was consistent with a rate-determining CO_2-coordination step.[34] Likewise, the unity of KIE was also observed when the CoPc was immobilized within a non-coordinating poly-2-vinylpyridine polymer (P2VP). On the contrary, the five-coordinate CoPc(py) exhibited a primary KIE of 3.1, indicating a changed RDS involved in proton transfer. Moreover, the primary KIE of *ca.* 2 was observed on the five-coordinate CoPc(py) immobilized within P2VP and parent CoPc immobilized within the coordinating polymer P4VP, suggesting that the PVP polymers moderated the extent of KIE for the five-coordinate CoPc systems with axially-ligated pyridyls. These findings prove that axial-coordination from the pyridyl moieties in P4VP to CoPc changes the RDS in CO_2 electroreduction, resulting in the increased activity.[178] Moreover, Guo and co-workers reported a primary KIE of 4 over copolymerization of CoPc supported on CNT in H-type cell in electrocatalytic CO_2 reduction to CO, indicating proton transfer was involved in RDS. Further modification with ultrathin conjugated microporous phthalocyanines (Pc) layer (CNT@CMP(H_2PCCoPc)) significantly decreased KIE to *ca.*1.8, signifying that the water dissociation was largely accelerated with the assistance of the H_2Pc layer. Interestingly, the as-prepared CNT@CMP(H_2PC-CoPc) enabled a maximum of 97% at a current density >200 mA cm^{-2} at -0.9 V *vs.* RHE.[179] Similar strategies for CoPc were also reported in other studies.[128,180]

3.3.3 The problems and challenges in KIE study. Although H/D KIE studies are widely investigated to provide useful information for reaction mechanisms, several problems and challenges in experimental design and measurement need to be addressed. For example, non-labeled proton sources (*e.g.*, OH^- and HCO_3^-) in the electrolyte must be replaced independently with deuterium to effectively and accurately conduct and interpret H/D KIE studies. It should be noted that the KIE effect can be intertwined with isotope effects related to mass transport, resulting from differences in the diffusion of D_2O or the acid dissociation constants. Hence, apart from H in the electrolyte, all other local reaction microenvironments (*e.g.*, temperature, solvation effects, CO_2 transportation) should be

identical. In this case, GDE is recommended for use. Finally, any presence of H_2O on the surface of the electrode from the atmosphere can affect the obtained KIE, especially in systems with secondary KIE or inverse KIE.

3.4 Temperature-sensitivity analysis of electrochemical $CO_{(2)}$ reduction

Until now, GDE has already been used to increase the current densities of $CO_{(2)}$ reduction to industrially relevant values. However, the energy efficiency of electrochemical reactions (defined by comparing the applied voltage with the thermodynamic voltage) is much worse than the required efficiency. Increasing operating temperature is an effective strategy, which generally results in higher rates and increases the energy efficiency.[181–183] However, systematical temperature-sensitivity analysis is rare and the temperature effect in electrocatalytic CO_2 reduction is complex, which can affect several reaction parameters, including local pH, the diffusion rate of reactants to the electrode surface, adsorbed intermediates, and solution resistance.

Hori *et al.* investigated the temperature dependent-performance over PC–Cu in electrocatalytic CO_2 reduction using a H-type cell, where the catalytic performance was evaluated at a constant current density of 5 mA cm^{-2}. The electrode potential was decreased from −1.39 to −1.33 V *vs.* SHE with an increase of temperature from 0 to 40 °C. The results showed that CH_4 was the dominant product at 0 °C, and its maximum faradaic efficiency (FE) was 60%. With increasing temperatures to 40 °C, the H_2 evolution and C_2H_4 formation dominated the surface reaction and the corresponding FE was 50% for H_2 and 20% for C_2H_4.[184] It is noteworthy that the catalytic performance was obtained during the first 15 min. Consistently, Ahn *et al.* also found that lower temperature (2 °C) favored CH_4 formation (*ca.* 50%) at the expense of C_2H_4 (only 10%) and H_2 evolution dominated the electrochemical reaction in H-type cell, reaching >50% FE_{H2} at >30 °C at an applied potential of −1.60 V *vs.* Ag/AgCl. Temperature effects were explained mainly by the changes in CO_2 concentration rather than changes in pH.[185] However, it was also reported that lower temperature favored CH_4 and C_2H_4 generation over Cu-based catalysts in KOH + methanol due to the higher CO_2 solubility.[184,186,187]

The temperature-sensitivity analysis will be more interesting at commercially-relevant current densities, which can be used for system design. Löwe *et al.* investigated the temperature dependence on tin oxide loaded GDE in electrocatalytic CO_2 reduction to formate. As the temperature increased, the total current density was enhanced (Fig. 9a). Considering the selectivity, the best performance was achieved at a temperature of 50 °C, which allowed a current density of 1000 mA cm^{-2} with FE_{HCOO^-} >80%. Lower or higher operating temperatures both show an increased HER at total current density of 1000 mA cm^{-2}, likely resulting from the opposing influence of temperature on CO_2 diffusion coefficients and solubility in the water layer on Cu. Note that electrowetting needs not to be considered when increasing the temperature for electrolysis.[188]

In addition, Zhuang and co-workers investigated the temperature-dependent performance of PC-Au and the efficiency of CO_2 reduction to CO in an alkaline polymer electrolyte using pure water as the electrolyte. When the operating temperature was increased from 30 °C to 80 °C, the FE_{CO} declined from 96% to 72% and the cell voltage decreased from 2.5 V to 2.2 V (Fig. 9b), resulting from the kinetic effects of both the electrode reactions and the ionic conduction.[189] Since solution resistance was less than 0.4 Ω cm^{-2}, the corresponding voltage reduction was only 0.04 V. Hence, the improvement mainly comes from the reaction kinetics rather than the ionic conduction. The decline in the FE_{CO} upon increased temperature indicated the change in the catalytic selectivity between CO_2 reduction and HER. These studies suggest that exploring the optimal operating temperature is essential to increase energy efficiency. Importantly, GDE restructuring and membrane failures were observed at high operating temperatures, leading to severe deactivation of the catalytic systems.[190–194]

Although the trend of CO_2 electroreduction has been examined in some systems, the apparent activation energy (E_a) was rarely calculated, which is a quantitative analysis of temperature effects. Kim *et al.* examined the temperature-dependent performance from 303 to 343 K over Ag NPs and Ni–N/C separately in a membrane electrode assembly electrolyzer (MEA) and the corresponding E_a of CO_2 reduction to CO and HER was calculated. The E_a of HER (45–60 kJ mol^{-1}) was always higher than that of CO evolution (10–20 kJ mol^{-1}) on both electrocatalysts (Fig. 9c and d). Moreover, Ni–N/C delivered a lower E_a of CO evolution (10 kJ mol^{-1}) than Ag NPs (20 kJ mol^{-1}), indicating that CO_2 activation was easier than that on Ag.[195] Of note, the E_a value was calculated by Arrhenius plots of j_{CO} and j_{H_2} at fixed −2.75 V, where the precise potentials were not well calibrated. In another study using H-type cell equipped with a reference electrode, the E_a of CO_2 reduction to CO over Ag NPs was 72 kJ mol^{-1}, much higher than that in MEA. Moreover, they found that different nanostructured Ag delivered different E_a values, where 44 kJ mol^{-1} and 21 kJ mol^{-1} were extracted for Ag rods and needles, respectively. These differences likely come from the local reaction environment and the calibration of applied potentials.

Koper and co-workers examined the temperature effects on rotating ring gold disk electrode in cation-promoted CO_2 reduction, disclosing that both activity and selectivity of CO_2 reduction to CO increased with temperature. However, the enhancement of kinetics of CO evolution was counteracted by the lower CO_2 solubility, which yielded an optimized working temperature of *ca.* 55 °C. The apparent activation energy was obtained to be 61 kJ mol^{-1} in 0.1 M $NaHCO_3$, whose value decreased with cation concentration and identity. In addition, the transfer coefficient was also derived to be *ca.* 0.3, which indicated that the enthalpy contribution played a dominant role in this process and entropy was non-negligible.[196]

Recently, Lu *et al.* investigated the temperature-sensitivity analysis of electrochemical CO reduction on Cu in a gas-fed flow cell equipped with a well-defined reference electrode, revealing a pronounced influence on the catalytic activity of CO reduction at increased temperatures. The calculated E_a values for all C_{2+} products fall within 60 ± 12 kJ mol^{-1},

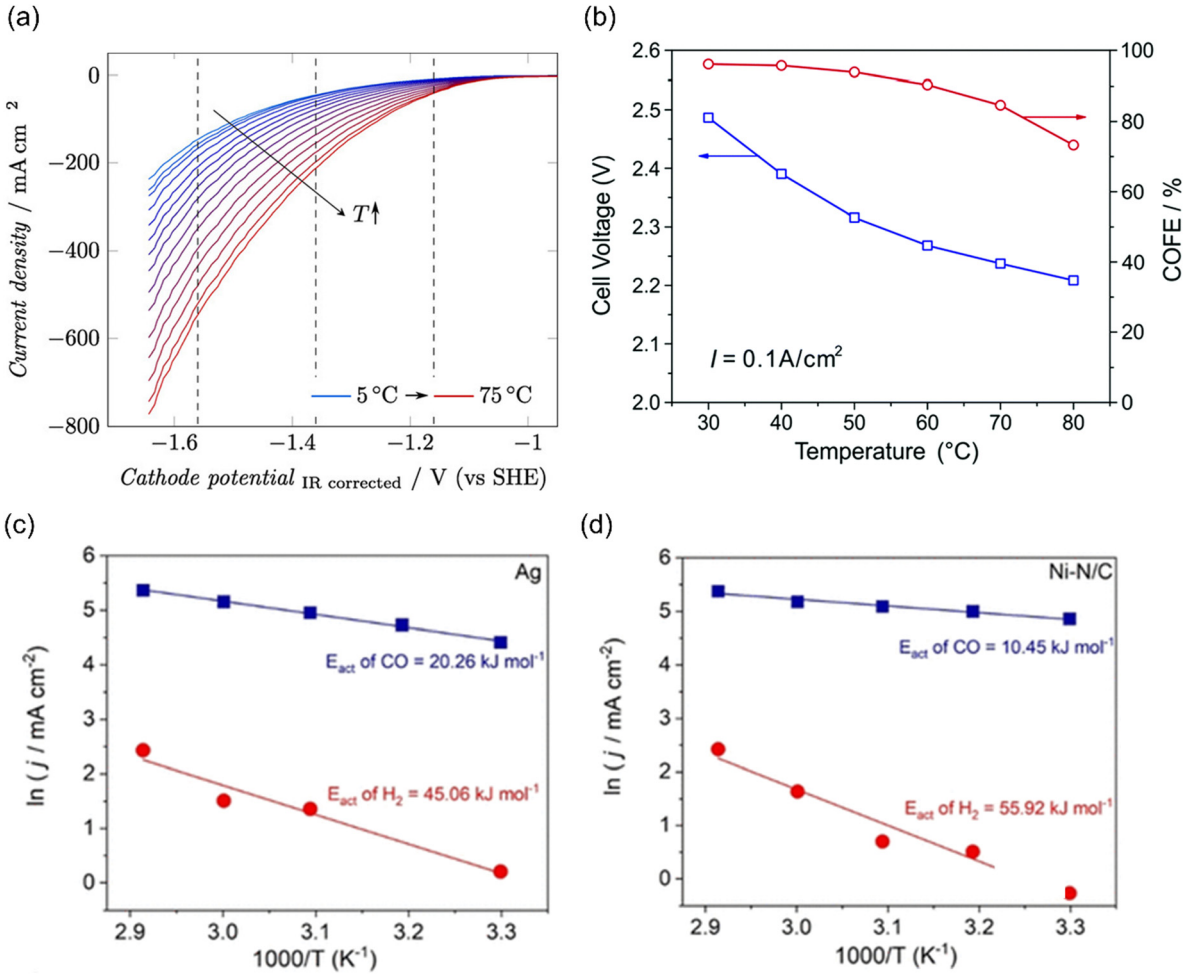

Fig. 9 (a) The temperature dependence on GDE of SnOx in a gas-fed flow cell. Reproduced with permission.[188] Copyright 2019, Wiley-VCH. (b) The temperature-dependent cell voltage and CO selectivity over Au under a current density of 0.1 A cm^{-2}. Reproduced with permission.[189] Copyright 2019, RSC publishing group. The activation energy for CO_2 reduction to CO (blue) and the HER (red) on (c) Ag and (d) Ni–N/C electrodes. Reproduced with permission.[195] Copyright 2021, American Chemical Society.

comparable to the reported theoretical value for the C–C coupling process of 30–75 kJ mol^{-1}.[154] It should be explicitly noted that the E_a value for each product did not have to reflect the (apparent) activation energy of the RDS, especially when the RDS followed selectivity-determining steps. Likewise, in reaction order analysis, various E_a values for each product were obtained, although they shared with a common RDS because the product distribution was perturbed by CO coverage as a key intermediate at selectivity-controlling steps after the RDS.

4. Challenges and limitations of microkinetic analysis in electrocatalytic $CO_{(2)}$ reduction

4.1 The existing challenges in microkinetic analysis

4.1.1 The measurements of intrinsic reaction kinetics. To accurately interpret microkinetic analysis, the intrinsic reaction rates must be extracted under experimental reactions, where the contribution of mass transport should be effectively isolated. Moreover, ECSA-normalized current densities are highly recommended in microkinetic analysis, which is the closest to the intrinsic activity without mass transport limitations.[197,198] Regarding the configuration of electrochemical reactors, the partial current densities of electrocatalytic CO reduction over Cu-based GDEs[145,149,150,199,200] when normalized to the geometric area or ECSA in the gas-fed flow cell or MEA are more than one or two orders of magnitude higher than that examined in H-type cell at similar overpotentials and bulk electrolyte conditions, ascribed to circumventing the gaseous CO diffusion-limitation, as shown in Fig. 10a. Moreover, the electrocatalytic performance of CO reduction and as-obtained reaction orders with respect to P_{CO} in the gas-fed flow cell and MEA are comparable (Fig. 10b), indicating the similarity of their local environment. Accordingly, a conventional H-type cell is not a good choice for microkinetic analysis in electrochemical $CO_{(2)}$ reduction. Although GDE likely mediates mass transport limitation during CO reduction, more detailed work is necessary to quantitively describe the diffusions of gas and electrolyte at electrode/electrolyte interfaces. Overall,

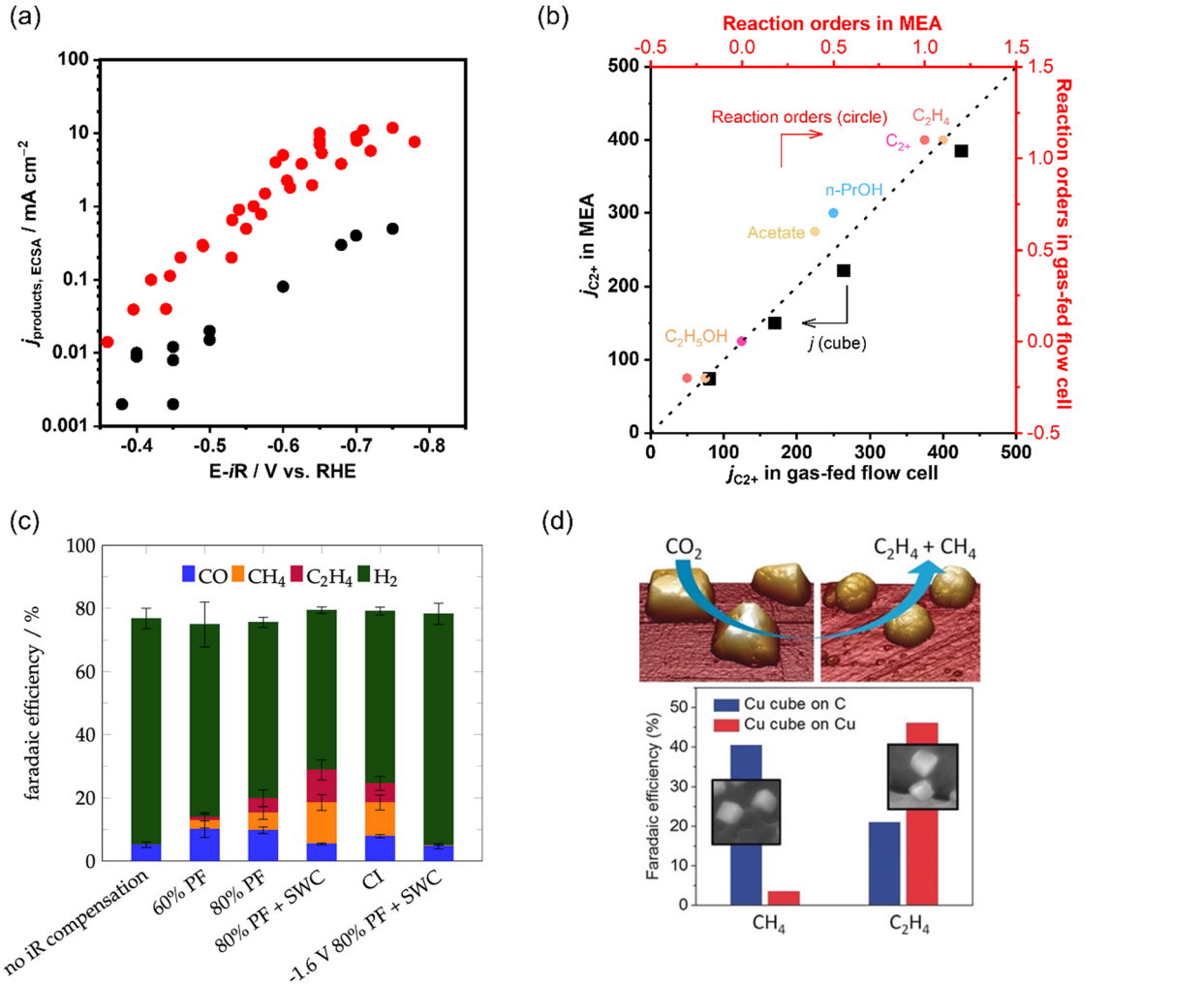

Fig. 10 (a) Comparison of C_{2+} partial current densities normalized to ECSA of CO electroreduction on Cu in a gas-fed flow cell and H-type cell. The data is adapted from ref. 145, 149, 150, 199, 200 (b) Comparison of as-obtained kinetic results ($j_{C_{2+}}$ and reaction orders) in a gas-fed flow cell and MEA under the same reaction conditions during CO electroreduction over Cu. The data is adapted from ref. 145. (c) Product distributions with different *i*R compensations at −1.7 V *vs.* Ag|AgCl in CO_2 saturated 0.1 M $KHCO_3$. Reproduced with permission.[204] Copyright 2022, American Chemical Society. (d) Dynamic changes in the structure and catalytic selectivity of Cu nanocubes in CO_2 electroreduction. Reproduced with permission.[205] Copyright 2018, Wiley-VCH.

an advanced model system with well-defined electrode and mass transport is highly desired for fundamental kinetic analysis. Voltage matters for intrinsic performance measurements and the readers are referred to the previous perspective for further details.[201] In addition, it should be highlighted that *i*R correction needs to be done appropriately to present the intrinsic activity and then use the polarization curves for Tafel analyses.[202] In the literature, different catalytic performances over the same electrocatalysts under similar reaction conditions were observed for electrocatalytic CO_2 reduction.[198] For example, FE_{CH4} varied significantly from *ca.* 6% at −1.0 V *vs.* RHE to 40% at −1.1 V *vs.* RHE in H-type cell,[203,204] indicating that small differences of tens of mV between the reported potential and the actual electrode potential could result in significant variations in the product distribution. Moreover, ionic conductivity also changed during electrolysis experiments due to the ion-selective membranes, indicating that the actual electrode potential always changed unless continuous *i*R measurement and compensation were applied.[204] Additionally, various types of *i*R compensation on PC–Cu for electrocatalytic CO_2 reduction in the same setup would also lead to different potentials at the cathode, they also have a direct impact on the observed current density (Fig. 10c). Both the current interrupt and the 80% positive feedback by software correction methods were shown to keep the actual potential closest to the desired potential throughout the potentiostatic electrolysis runs. Thus, using the most robust approach to measuring and reporting the results is necessary.

4.1.2 Dynamically restructured electrocatalysts. An additional challenge in the microkinetic analysis is that dynamic changes in the structure and catalytic selectivity of electrocatalysts occur in CO_2 electroreduction (Fig. 10d).[205] In electrocatalytic $CO_{(2)}$ reduction, both the negatively applied potentials and the strong surface–absorbate interactions can lead to

catalyst surface restructuring and further significant changes, resulting in changing performance.[206–208] For example, the dynamic morphological changes of Cu have been demonstrated *via* operando X-ray absorption spectroscopy (XAS) and *in situ*/*ex situ* transmission electron microscopy (TEM),[209] where some under-coordinated sites formed to accelerate CO_2 reduction and induce different selectivity.[210,211] The dynamical evolution of edge and stepped sites facilitated the electroreduction of CO_2 to C_2H_4 and ethanol over Cu_2O film.[212] Potential-induced active-sites formation was also reported on CuPc *via* operando XAS, where a reversible transformation between isolated Cu atoms and Cu_n clusters was captured.[213] Similar surface-morphological-change induced active-sites formation have been also observed on non-copper-based catalysts, including S-doped Cu, Ag, and InN.[214–216] Overall, electrocatalysts may undergo morphology reconstructions, such as dissolution, redeposition, and leaching, and further lead to changes in selectivity and activity. To obtain reasonable microkinetic results, electrocatalyst stability must be carefully considered.

4.1.3 The complexity of electrolyte effects. Beyond the identity of the electrocatalyst materials, the nature of the electrolyte including cation identity and pH can strongly affect the catalytic performance (activity, selectivity, and stability in GDE electrolyzers). Several potential contributions of cations during $CO_{(2)}$ reduction have been put forward.[37,63,133,217–222] One commonly accepted pathway is that cations facilitate the surface-mediated $CO_{(2)}$ reduction by modifying the interfacial electric field *via* cation-noncovalent interactions on the electrode surface.[131,133] For example, Ringe *et al.* established a multi-scale modeling approach that combined size-modified Poisson–Boltzmann theory with *ab initio* simulations of field effects on key reaction intermediates to provide quantitative evidence for the impact of cations on the interfacial electric field, as shown in Fig. 11a.[131] Besides this interfacial electric field effect, Koper and coworkers extensively investigated cation effects in CO_2 electroreduction to CO under well-defined mass transport conditions.[221] Their results coupling online product-detection experiments and theoretical calculations suggested that the partially desolvated metal cations participate in the formation of CO_2–intermediate *via* a short-range electrostatic interaction (Fig. 11b), which provided definitive evidence that cations could stabilize the crucial reaction intermediate on gold, silver, or copper. In addition, Xu and coworkers utilized *in situ* surface-enhanced spectroscopic investigations to suggest that not only the change of interfacial electric field strength with cation size but also the presence of a nonelectric field

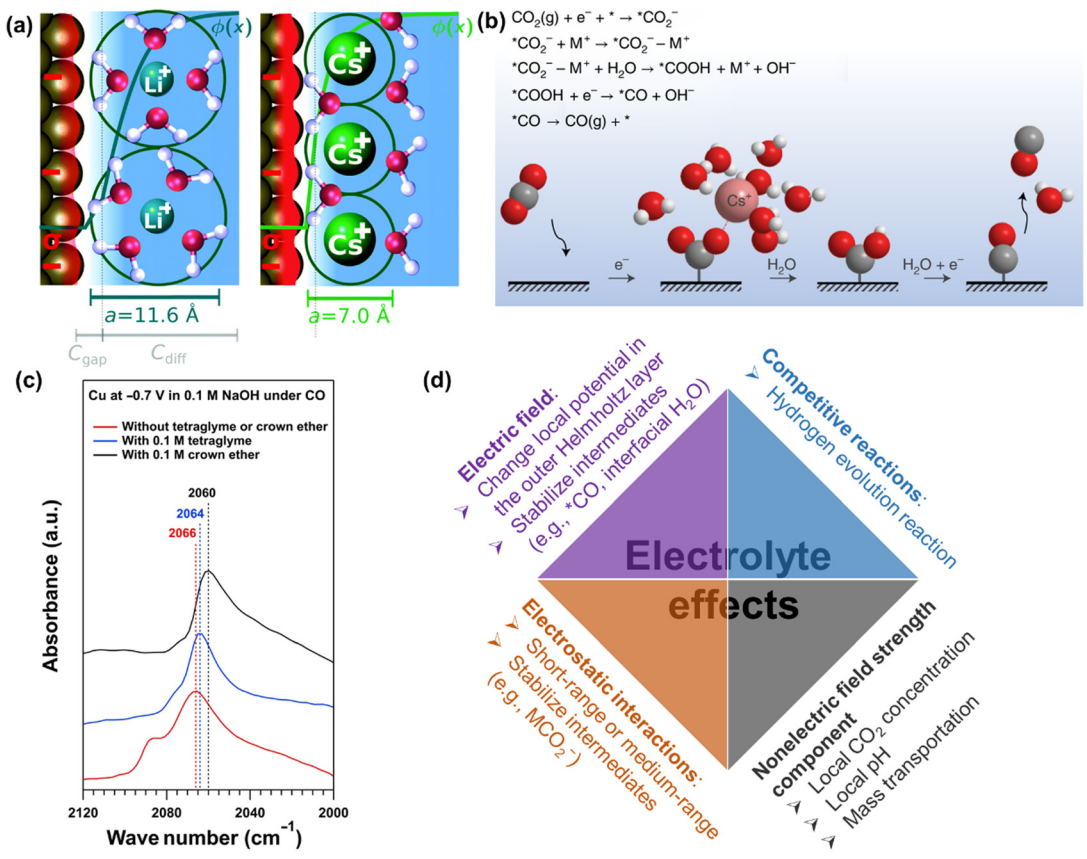

Fig. 11 (a) Illustration of the origin of cation effects in field-driven electrocatalysis. Reproduced with permission.[131] Copyright 2019, RSC publishing group. (b) Schematic representation of the interaction of the cation with the negatively charged CO_2^- intermediate together with a proposed reaction mechanism. Reproduced with permission.[221] Copyright 2021, nature publishing group. (c) The impact of organics on attenuated total reflection surface-enhanced infrared absorption spectroscopy.[133] (d) Summary of electrolyte effects on electrochemical CO_2 reduction.

strength component, especially the environment around alkali metal cations (chelating agent, hydration shells, or the interfacial water, affected the CO reduction on Cu.[133] Spectroscopic investigations with cation chelating agents and organic molecules (Fig. 11c) exhibited that the electric and nonelectric field components of the cation effect could be affected by both cation identity and composition of the electrochemical interface.[133]

Furthermore, the nature and concentration of anions also influence the performance by their effects on the competing HER, especially in the presence of mass-transportation conditions.[223–226] Since the different branches of HER (*e.g.*, proton, buffer mediated species, or water reduction) on electrocatalysts could occur depending on the local reaction microenvironments including applied potentials, the concentration of electrolyte, and $CO_{(2)}$ concentration. For more detailed reviews of electrolyte effects on CO_2 electrochemical reduction, the reader is referred to specialized recent reviews.[222]

Overall, the last decades have witnessed intensive research efforts dedicated to the exploration of electrolyte effects on $CO_{(2)}$ reduction, as illustrated in Fig. 11d. Nevertheless, their main role (especially cation) is still under discussion. For example, Li *et al.* revealed that a small change in interfacial electric field strength was not likely the main contribution to the as-obtained difference in the performance of CO reduction, where the varying interaction between adsorbed CO and interfacial water was interpreted to change performance in presence of different organic cations.[227] Similarly, Xu and co-workers reported that the cation concentration (*e.g.*, 0.1 M or 1 M Na^+) and cation identity (*e.g.*, K^+, Rb^+, Cs^+) during CO reduction did not change the Stark tuning rate or the interfacial electric field strength;[133,220] on the contrary, they significantly changed the catalytic performance. Then, nonelectric field strength components of the cation effect were proposed to affect CO dimerization.[133] However, the definitive evidence of nonelectric field strength components is still missing. Thus, systematic studies of the cation effects on $CO_{(2)}$ reduction and the correspondingly quantitative expression in kinetic equations are necessary for further study.

4.2 Limitations of the microkinetic analysis

4.2.1 The coverage of the adsorbed species assumptions in microkinetic analysis. In the Tafel slope and reaction order analysis, extreme coverage of the adsorbed species ($\theta \approx 0$ or ≈ 1) is generally assumed, although, in practice, the slopes are coverage dependent. For example, it is widely accepted that the Tafel slopes of 120, 40, and 30 mV dec^{-1} are observed for the Volmer, Heyrovsky, and Tafel determining rate steps, respectively, during HER. However, for the Heyrovsky rate-determining step, a Tafel slope of 120 mV dec^{-1} was observed in the higher adsorbed hydrogen atom coverage ($\theta_H > 0.6$). Similarly, the Tafel slope of CO_2 electroreduction toward CO could be simplified to eqn (10), when a3 is assumed to be RDS.

$$b = \frac{2.3RT}{F(\alpha + \theta_1 + \theta_2)} \quad (10)$$

where θ_1 and θ_2 are the coverage of *COOH and *COOH–H^+, respectively. Hence, the first electron transfer limiting the reaction rate does not necessarily showing an experimentally observed slope of 120 mV dec^{-1} and there are other potential scenarios.

In addition, reaction order is also coverage dependent. For example, it has been demonstrated that the coverage of the intermediates was changing based on the applied potentials in CO electro-oxidation, resulting in the changed reaction orders along with the applied potentials. Therefore, it is challenging to use only the Tafel slope and reaction order to affirm or exclude a proposed mechanism without any information on the coverage of intermediates under operating conditions in electrocatalytic $CO_{(2)}$ reduction.

To understand the coverage of intermediates, future work involving surface-sensitive spectroscopies mirroring GDE based-conditions is needed. For example, Lu and co-workers developed a custom-designed spectra-electrochemical cell allowing CO pressures up to 6 MPa to investigate surface enhanced infrared spectroscopy over PC–Cu in electrocatalytic CO reduction. They found the upper bound of the CO coverage under electrocatalytic conditions to be 0.05 monolayer at atmospheric pressure and the saturation CO coverage to be $\sim$0.25 monolayer.[139] Apart from operando spectroscopies, DFT is another convenient and powerful tool to understand the adsorption isotherm for relevant adsorbates and thermodynamic parameters related to the adsorption equilibrium constant.

It is also worth mentioning that the effect of the applied potential on the free energy of intermediates is important since the enthalpy and entropy of intermediates are potential-dependent in many cases.[153] Wang and co-workers developed a continuous-flow Raman electrochemical cell for electrocatalytic CO_2 reduction, which enabled to monitor the local pH variation near the surface of GDE under reaction conditions,[228] verifying the presence of the apparent overpotential reduction on the RHE scale in alkaline electrolyte due to the Nernst potential of the strong pH gradient layer at the cathode/electrolyte interface. This change in the electric fields can significantly alter the binding energies of intermediates and solvent molecules at the electrode/electrolyte interface. In addition, the adsorption energy of intermediates can also be affected by the coverages of adsorbates on the surface.

Overall, the coverage of various intermediates should not be overlooked in both the Tafel slope and apparent reaction order analysis, where the electric field effects and adsorbate–adsorbate interactions may be necessary to consider.

4.2.2 Other assumptions in the microkinetic analysis. In microkinetic analysis, we always assume a transfer coefficient α of 0.5 in an elementary charge-transfer step. Indeed, it is not necessary to be 0.5[229] and has been identified as a function of the electrode potential, especially in organic systems using acetonitrile or dimethylformamide as a solvent containing quaternary ammonium salt as supporting electrolytes.[230] For the reduction of benzaldehyde in ethanol, the potential dependent α examined by potential-sweep voltammetry can be written

as the following eqn (11):

$$\frac{\partial \alpha}{\partial E} = \frac{F}{4\lambda}\left(1 - \frac{\partial \varphi_r}{\partial E}\right) \quad (11)$$

where λ is the solvent reorganization factor, relating to the transition state; φ_r is the potential difference between the reaction site and the solution.[230] Similarly, the α can also be predicted from 1D potential energy surface based on Marcus theory of outer-sphere electron transfer, where the reactant and product do not interact directly with the electrode surface; the detailed expression can be simplified as follows:[29,88]

$$\alpha = \frac{1}{2} + \frac{F\eta}{2\lambda} \quad (12)$$

Consistently, α is mainly governed by overpotential and solvent reorganization. Only when $\lambda \gg \eta$, α = 0.5. In addition to the organic system, some significant deviation values from 0.5 have been observed in some aqueous electrochemical reactions, for example, Cr(ethylenediamine)$_3^{3+}$ reduction on the Pb–Ag surface.[231] Moreover, the electrode properties (*e.g.*, pore structures and ionic or electronic conductivity) and a high exchange current density were reported to cause α to be <0.5 in the oxygen reduction reaction.[232] These will dramatically impact the calculated values of the Tafel slopes and apparent activation energy.

An additional assumption in microkinetic analysis pertains to the quasi-equilibrium, where the reactions are assumed to occur rapidly in both forward and reverse directions before the RDS step. Actually, the non-rate-determining step can be nonequilibrium. In oxygen evolution reaction, Marshall *et al.* have demonstrated that models using the quasi-equilibrium assumption fail to predict some Tafel regions.[233] Hence, the steady-state assumption is recommended for predicting Tafel slopes.

4.2.3 Theoretical models in DFT calculation. Although DFT calculations have been widely utilized to probe all intermediates at the atomic level and provide deeper insights into reaction pathways, varied theoretical models always present different pictures for $CO_{(2)}$ reduction.[234–236] The last decades have witnessed intensive research efforts dedicated to this direction. For example, the pioneering work by Nørskov *et al.* proposed the computational hydrogen electrode (CHE) model, pushing the huge development of modeling electrochemical processes. Based on this model, Peterson *et al.* first reported the detailed reaction mechanism on Cu(211) surface, in agreement with the experimentally as-obtained onset potentials of the major products.[237] However, owing to the oversimplification in this model, computational results sometimes deviated from the experiments.[238] Afterwards, the implicit and explicit solvent models were established to describe solvent effects in the catalyst surface/electrolyte interfaces.[239] To exhibit more dynamic water layers in the electrochemical interface, *ab initio* molecular dynamics (AIMD) simulations have been widely used to improve the reliability of modeling.[238,240] Furthermore, the applied potential was considered in the homogeneous background or linearized Poisson–Boltzmann model to simulate electrified interfaces.[241] Alternatively, the quantum mechanics(QM)/molecular mechanics (MM) model was reported to describe the interface between QM and MM regions, which became the key to obtaining accurate results.[242,243] Despite great progress, it still remains challenging that the complexity of the electrochemical interface between electrocatalysts and electrolyte remains elusive and could not be taken into consideration in one model. For example, $CO_{(2)}$ reduction under practical conditions generally occurs at a constant potential with an infinite reservoir of electrons; however, in the simulations, the reservoir of electrons is finite; the cations have unknown and non-negligible effects on $CO_{(2)}$ reduction at the electrochemical interface. Fortunately, the huge development of machine learning is likely to be a revolutionary approach for the simulation of $CO_{(2)}$ reduction on a larger space and time scale.[244,245]

5. Conclusion and outlook

Microkinetic studies are powerful tools in electrocatalytic $CO_{(2)}$ reduction, helping to identify critical reaction intermediates and RDSs. This information is crucial for designing improved electrocatalysts and scaling up $CO_{(2)}$ electrochemical reactors. This review systematically summarizes DFT-based microkinetic models for various products (*e.g.*, CO, HCOOH, CH_4, and C_{2+}) and numerous experimentally-derived kinetic observables associated with the complex processes occurring in electrocatalytic $CO_{(2)}$ reduction. Although Tafel and reaction order analyses, combined with KIE and temperature sensitivity analyses, are widely used to gain mechanistic insights, the kinetic observables obtained under incorrect operating conditions or oversimplified models often fail to accurately describe surface electrocatalysis. The experimentally scattered results have been systematically analyzed, and the effect of the local reaction microenvironment on the obtained kinetic observables has been highlighted. Moreover, the challenges in intrinsic kinetic measurements and the limitations of microkinetic analysis are carefully discussed.

With these challenges and limitations in mind, we now consider the opportunities for more effectively using microkinetic analysis to understand the reaction mechanism. The detailed strategies are as follows:

(1) Accurate interpretation of catalytic performance

Selecting well-defined electrodes, suitable experimental conditions, and reactor configurations is critical for intrinsic kinetic measurements, where the measured rates are governed by kinetics rather than being convoluted by mass transport limitations. And no mass transport limitation in the system and potential/time-independent electrodes are required. In this context, the rotating ring disk electrode (RRDE) is a potential candidate to extract the true intrinsic kinetics of electrocatalysts, which has been successfully demonstrated to control and improve mass transport for oxygen reduction reaction. For CO_2 reduction to CO, Koper and coworkers have utilized RRDE to perform microkinetic analysis over Au in various electrolytes

under well-defined mass transport conditions and using online analytical techniques.[71,222–224] In further work, the well-defined RRDE equipped with online product identification (*e.g.*, H_2, $HCOO^-$, CH_4, C_{2+}) and quantification techniques with high resolution will be the next system challenges. Alternatively, the exploration of well-defined electrodes with the gas-diffusion layer will be another direction, which allow for higher current densities. Accordingly, the commonly used online analytical techniques can be used. It should be noted that this configuration absolutely will introduce non-kinetic effects including the complexities of electrode/electrolyte interfaces and diffusion processes of liquid and gas, where it needs more efforts to quantitatively describe their corresponding contributions to the as-obtained catalytic performance. Moreover, as Koper and co-workers recommended in the rigorous Tafel analysis of oxygen evolution reaction, Tafel slopes should be plotted *versus* current densities or applied potentials to yield a kinetically meaningful Tafel slope value, which was obtained from a horizontal Tafel slope region.[246]

In addition, special care is also needed that catalytic performance of electrocatalyst material will be assessed at commercially relevant current densities, not only substantially lower ones since it is strongly influenced by not only the identity of the electrocatalyst materials but also the local steady-state environment perturbed by reaction micro-environment and the operating current density. Apparent kinetic parameters are necessary to be utilized to establish the relationship between the intrinsic kinetics and ''apparent kinetics'' at commercially-relevant conditions, which could accelerate the technology toward large-scale $CO_{(2)}$ reduction. Consequently, the GDE with a well-defined reference electrode is needed to alleviate mass transport limitations and record the actual applied potentials. It should be mentioned that the stability of electrocatalysts during electrolysis is of great importance. Electrocatalysts with structural simplicity, ease of handling, and robustness are particularly attractive for fundamental kinetic studies. To enhance stability, one recent example involves placing an inactive material atop the catalyst layer as a current collector, preventing both catalyst restructuring and deposition of contaminants on the active catalyst surface.[247] Finally, accurate and precise reporting for electrochemical CO_2 reduction studies is essential. For instance, *i*R compensation should be carefully corrected, and the measured rates should be normalized to the geometric electrode area as well as the ECSA. For further details on standards and protocols for data acquisition and reporting, readers are referred to previous studies.[114,248]

(2) Utilizing operando spectroscopies as complementary tools

Due to the complexities and uncertainties of microkinetic analysis, it remains challenging to rely solely on microkinetic models to fully uncover reaction mechanisms. Operando spectroscopies can be employed as complementary tools to increase reliability, such as attenuated total reflection surface-enhanced infrared spectroscopy (ATR-SEIRAS),[136,137,139] operando Raman spectroscopy,[249–251] ambient-pressure X-ray photoelectron spectroscopy,[252] and differential electrochemical mass spectroscopy.[253] In particular, *in situ*/operando techniques with high resolution in the time frame of below second is helpful to capture the short-lifetime intermediate. In addition, surface-sensitive spectroscopies that mirror GDE based-conditions (at high rates) are highly desirable, requiring a careful design and fabrication of dedicated devices.

(3) Improving DFT-based microkinetic simulation

Significant process in DFT calculations has been made in recent years. Electrochemical activation barriers and potential contributions from electric fields and solvation effects are now considered in microkinetic modeling to enhance computational accuracy. However, an additional constraint stemming from DFT relates to the assumptions of the microkinetic model itself, such as the quasi-equilibrium assumption and random distribution of adsorbed species on the catalytic surface in mean-field models.[12,233] As discussed, oversimplified assumptions can lead to misleading conclusions about reaction mechanisms. Therefore, the steady-state assumption is recommended. Several non-idealities should be addressed in future microkinetic modeling, including interfacial structures, solvent dynamics, potential-dependent symmetry factors, potential-dependent intermediate coverage, and adsorbate–adsorbate interactions.

(4) Strengthening the connection between DFT and experiments

Strengthening the connection between DFT and experiments is crucial for accurately understanding the mechanistic details of electrocatalytic $CO_{(2)}$ reduction and designing novel electrocatalysts,[25,254] which could accelerate the data-driven screen and design of electrocatalysts. Accordingly, the iterative model refinement can be employed as a general methodology. First, the establishment of a model system is an important part of DFT calculation where the correspondingly active site is needed to construct based on fundamental physical and chemical characterizations, but also the electrochemical microenvironment around active sites as well as electrode potential is crucial to be considered. To reduce the complexity in formulating electrochemical processes, single-crystal materials[76,196,221–223,226,255] and surface-immobilized single-site catalysts[256,257] are highly recommended. Second, kinetic observables are extracted from experiments without mass transport limitation to optimize DFT-based parameters and achieve consistency between computation and experiments. Finally, the feedback gained from the parameter adjustment process is used to revise the original hypothesis for the reaction mechanism and iterate all steps until consistency between experiments and computation is achieved, thereby accurately describing the nature of electrocatalysts.

Conflicts of interest

There are no conflicts to declare.

Acknowledgements

Asahi Kasei Corporation financially supported this work.

References

1 I. E. Stephens, K. Chan, A. Bagger, S. W. Boettcher, J. Bonin, E. Boutin, A. K. Buckley, R. Buonsanti, E. R. Cave and X. Chang, *J. Phys.: Energy*, 2022, **4**, 042003.
2 H. Shin, K. U. Hansen and F. Jiao, *Nat. Sustain.*, 2021, **4**, 911–919.
3 P. De Luna, C. Hahn, D. Higgins, S. A. Jaffer, T. F. Jaramillo and E. H. Sargent, *Science*, 2019, **364**, eaav3506.
4 S. Nitopi, E. Bertheussen, S. B. Scott, X. Y. Liu, A. K. Engstfeld, S. Horch, B. Seger, I. E. L. Stephens, K. Chan, C. Hahn, J. K. Norskov, T. F. Jaramillo and I. Chorkendorff, *Chem. Rev.*, 2019, **119**, 7610–7672.
5 Y. Y. Birdja, E. Pérez-Gallent, M. C. Figueiredo, A. J. Göttle, F. Calle-Vallejo and M. T. M. Koper, *Nat. Energy*, 2019, **4**, 732–745.
6 D. H. Nam, P. De Luna, A. Rosas-Hernandez, A. Thevenon, F. W. Li, T. Agapie, J. C. Peters, O. Shekhah, M. Eddaoudi and E. H. Sargent, *Nat. Mater.*, 2020, **19**, 266–276.
7 J. Resasco and A. T. Bell, *Trends Chem.*, 2020, **2**, 825–836.
8 J. A. Rabinowitz and M. W. Kanan, *Nat. Commun.*, 2020, **11**, 5231.
9 A. Ozden, Y. H. Wang, F. W. Li, M. C. Luo, J. Sisler, A. Thevenon, A. Rosas-Hernandez, T. Burdyny, Y. W. Lum, H. Yadegari, T. Agapie, J. C. Peters, E. H. Sargent and D. Sinton, *Joule*, 2021, **5**, 706–719.
10 T. Alerte, J. P. Edwards, C. M. Gabardo, C. P. O'Brien, A. Gaona, J. Wicks, A. Obradovi, A. Sarkar, S. A. Jaffer, H. L. MacLean, D. Sinton and E. H. Sargent, *ACS Energy Lett.*, 2021, **6**, 4405–4412.
11 O. S. Bushuyev, P. De Luna, C. T. Dinh, L. Tao, G. Saur, J. van de Lagemaat, S. O. Kelley and E. H. Sargent, *Joule*, 2018, **2**, 825–832.
12 A. Baz, S. T. Dix, A. Holewinski and S. Linic, *J. Catal.*, 2021, **404**, 864–872.
13 A. T. Marshall, *Curr. Opin. Electrochem.*, 2018, **7**, 75–80.
14 G. A. Cerrón-Calle, T. P. Senftle and S. Garcia-Segura, *Curr. Opin. Electrochem.*, 2022, 101062.
15 T. Shinagawa, A. T. Garcia-Esparza and K. Takanabe, *Sci. Rep.*, 2015, **5**, 1–21.
16 S.-Q. Xiang, S.-T. Gao, J.-L. Shi, W. Zhang and L.-B. Zhao, *J. Catal.*, 2021, **393**, 11–19.
17 Q. Li, Y. Ouyang, S. Lu, X. Bai, Y. Zhang, L. Shi, C. Ling and J. Wang, *Chem. Commun.*, 2020, **56**, 9937–9949.
18 J. T. Mefford, Z. Zhao, M. Bajdich and W. C. Chueh, *Energy Environ. Sci.*, 2020, **13**, 622–634.
19 G. O. Larrazábal, A. J. Martín and J. Perez-Ramirez, *J. Phys. Chem. Lett.*, 2017, **8**, 3933–3944.
20 Q. Lu and F. Jiao, *Nano Energy*, 2016, **29**, 439–456.
21 F. Dattila, R. R. Seemakurthi, Y. Zhou and N. López, *Chem. Rev.*, 2022, **122**, 11085–11130.
22 M. R. Singh, J. D. Goodpaster, A. Z. Weber, M. Head-Gordon and A. T. Bell, *Proc. Natl. Acad. Sci. U. S. A.*, 2017, **114**, E8812–E8821.
23 A. Bagger, W. Ju, A. S. Varela, P. Strasser and J. Rossmeisl, *Chem. Phys. Chem.*, 2017, **18**, 3266–3273.
24 M. Zhong, K. Tran, Y. M. Min, C. H. Wang, Z. Y. Wang, C. T. Dinh, P. De Luna, Z. Q. Yu, A. S. Rasouli, P. Brodersen, S. Sun, O. Voznyy, C. S. Tan, M. Askerka, F. L. Che, M. Liu, A. Seifitokaldani, Y. J. Pang, S. C. Lo, A. Ip, Z. Ulissi and E. H. Sargent, *Nature*, 2020, **581**, 178–183.
25 J. Resasco, F. Abild-Pedersen, C. Hahn, Z. Bao, M. Koper and T. F. Jaramillo, *Nat. Catal.*, 2022, **5**, 374–381.
26 M. Dunwell, W. Luc, Y. Yan, F. Jiao and B. Xu, *ACS Catal.*, 2018, **8**, 8121–8129.
27 C. W. Lee, N. H. Cho, S. W. Im, M. S. Jee, Y. J. Hwang, B. K. Min and K. T. Nam, *J. Mater. Chem. A*, 2018, **6**, 14043–14057.
28 T. Shinagawa, A. T. Garcia-Esparza and K. Takanabe, *Sci. Rep.*, 2015, **5**, 13801.
29 Y.-H. Fang and Z.-P. Liu, *ACS Catal.*, 2014, **4**, 4364–4376.
30 S. Fletcher, *J. Solid State Electrochem.*, 2009, **13**, 537–549.
31 J. Rosen, G. S. Hutchings, Q. Lu, S. Rivera, Y. Zhou, D. G. Vlachos and F. Jiao, *ACS Catal.*, 2015, **5**, 4293–4299.
32 S. Ringe, C. G. Morales-Guio, L. D. Chen, M. Fields, T. F. Jaramillo, C. Hahn and K. Chan, *Nat. Commun.*, 2020, **11**, 33.
33 M. Dunwell, Q. Lu, J. M. Heyes, J. Rosen, J. G. Chen, Y. Yan, F. Jiao and B. Xu, *J. Am. Chem. Soc.*, 2017, **139**, 3774–3783.
34 X. Lu, B. Dereli, T. Shinagawa, M. Eddaoudi, L. Cavallo and K. Takanabe, *Chem Catal.*, 2022, **2**, 1143–1162.
35 A. Wuttig, M. Yaguchi, K. Motobayashi, M. Osawa and Y. Surendranath, *Proc. Natl. Acad. Sci. U. S. A.*, 2016, **113**, E4585–E4593.
36 B. A. Zhang, T. Ozel, J. S. Elias, C. Costentin and D. G. Nocera, *ACS Central Sci.*, 2019, **5**, 1097–1105.
37 L. D. Chen, M. Urushihara, K. Chan and J. K. Nørskov, *ACS Catal.*, 2016, **6**, 7133–7139.
38 M. R. Singh, J. D. Goodpaster, A. Z. Weber, M. Head-Gordon and A. T. Bell, *Proc. Natl. Acad. Sci. U. S. A.*, 2017, **114**, E8812–E8821.
39 N. Gupta, M. Gattrell and B. MacDougall, *J. Appl. Electrochem.*, 2006, **36**, 161–172.
40 A. S. Varela, M. Kroschel, T. Reier and P. Strasser, *Catal. Today*, 2016, **260**, 8–13.
41 M. Dunwell, X. Yang, B. P. Setzler, J. Anibal, Y. Yan and B. Xu, *ACS Catal.*, 2018, **8**, 3999–4008.
42 J. Ryu, A. Wuttig and Y. Surendranath, *Angew. Chem., Int. Ed.*, 2018, **57**, 9300–9304.
43 Z. Mao and C. T. Campbell, *J. Catal.*, 2020, **381**, 53–62.
44 H. Prats and K. Chan, *Phys. Chem. Chem. Phys.*, 2021, **23**, 27150–27158.
45 X. Chang, S. Vijay, Y. Zhao, N. J. Oliveira, K. Chan and B. Xu, *Nat. Commun.*, 2022, **13**, 2656.
46 X. Song, L. Xu, X. Sun and B. Han, *Sci. Chin. Chem.*, 2023, **66**, 315–323.

47 B. Hasa, Y. Zhao and F. Jiao, *Annu. Rev. Chem. Biomol. Eng.*, 2023, DOI: 10.1146/annurev-chembioeng-101121-071735.
48 E. Pérez-Gallent, M. C. Figueiredo, F. Calle-Vallejo and M. T. M. Koper, *Angew. Chem., Int. Ed.*, 2017, **56**, 3621–3624.
49 I. V. Chernyshova, P. Somasundaran and S. Ponnurangam, *Proc. Natl. Acad. Sci. U. S. A.*, 2018, **115**, E9261–E9270.
50 J. Gao, H. Zhang, X. Guo, J. Luo, S. M. Zakeeruddin, D. Ren and M. Grätzel, *J. Am. Chem. Soc.*, 2019, **141**, 18704–18714.
51 P. Wei, D. Gao, T. Liu, H. Li, J. Sang, C. Wang, R. Cai, G. Wang and X. Bao, *Nat. Nanotechnol.*, 2023, 1–8.
52 N. J. Firet and W. A. Smith, *ACS Catal.*, 2017, **7**, 606–612.
53 Y. Hori, H. Wakebe, T. Tsukamoto and O. Koga, *Electrochim. Acta*, 1994, **39**, 1833–1839.
54 Y. I. Hori, *Mod. Aspects Electrochem.*, 2008, 89–189.
55 Y. Hori, I. Takahashi, O. Koga and N. Hoshi, *J. Mol. Catal. A: Chem.*, 2003, **199**, 39–47.
56 Y. Hori, I. Takahashi, O. Koga and N. Hoshi, *J. Phys. Chem. B*, 2002, **106**, 15–17.
57 Y. Hori, R. Takahashi, Y. Yoshinami and A. Murata, *J. Phys. Chem. B*, 1997, **101**, 7075–7081.
58 D. Xu, Y. Xu, H. Wang and X. Qiu, *Chem. Commun.*, 2022, **58**, 3007–3010.
59 Z. Bitar, A. Fecant, E. Trela-Baudot, S. Chardon-Noblat and D. Pasquier, *Appl. Catal., B*, 2016, **189**, 172–180.
60 H. Wu, Z. Li, Y. Liu, X. Zou, L. Yin and S. Lin, *Sustainable Energy Fuels*, 2021, **5**, 5798–5803.
61 E. Nurlaela, T. Shinagawa, M. Qureshi, D. S. Dhawale and K. Takanabe, *ACS Catal.*, 2016, **6**, 1713–1722.
62 S. Rasul, D. H. Anjum, A. Jedidi, Y. Minenkov, L. Cavallo and K. Takanabe, *Angew. Chem., Int. Ed.*, 2015, **54**, 2146–2150.
63 M. Liu, Y. Pang, B. Zhang, P. De Luna, O. Voznyy, J. Xu, X. Zheng, C. T. Dinh, F. Fan and C. Cao, *Nature*, 2016, **537**, 382–386.
64 S. Verma, Y. Hamasaki, C. Kim, W. Huang, S. Lu, H.-R. M. Jhong, A. A. Gewirth, T. Fujigaya, N. Nakashima and P. J. A. Kenis, *ACS Energy Lett.*, 2018, **3**, 193–198.
65 J. Li, I. Maresi, Y. Lum and J. W. Ager, *J. Chem. Phys.*, 2021, **155**, 164701.
66 S. Hanselman, M. T. Koper and F. Calle-Vallejo, *ACS Energy Lett.*, 2018, **3**, 1062–1067.
67 F. Calle-Vallejo and M. T. M. Koper, *Angew. Chem., Int. Ed.*, 2013, **52**, 7282–7285.
68 K. J. P. Schouten, Y. Kwon, C. J. M. Van der Ham, Z. Qin and M. T. M. Koper, *Chem. Sci.*, 2011, **2**, 1902–1909.
69 X. Liu, J. Xiao, H. Peng, X. Hong, K. Chan and J. K. Nørskov, *Nat. Commun.*, 2017, **8**, 1–7.
70 X. Y. Liu, P. Schlexer, J. P. Xiao, Y. F. Ji, L. Wang, R. B. Sandberg, M. Tang, K. S. Brown, H. J. Peng, S. Ringe, C. Hahn, T. F. Jaramillo, J. K. Norskov and K. R. Chan, *Nat. Commun.*, 2019, **10**, 32.
71 M. T. M. Koper, A. Z. Weber, K. Chan and J. Cheng, *Chem. Rev.*, 2022, **122**, 10579–10580.
72 H. H. Heenen, J. A. Gauthier, H. H. Kristoffersen, T. Ludwig and K. Chan, *J. Chem. Phys.*, 2020, **152**, 144703.
73 S. Vijay, W. Ju, S. Brückner, S.-C. Tsang, P. Strasser and K. Chan, *Nat. Catal.*, 2021, **4**, 1024–1031.
74 J. T. Feaster, C. Shi, E. R. Cave, T. Hatsukade, D. N. Abram, K. P. Kuhl, C. Hahn, J. K. Nørskov and T. F. Jaramillo, *ACS Catal.*, 2017, **7**, 4822–4827.
75 M. T. Tang, H. Peng, P. S. Lamoureux, M. Bajdich and F. Abild-Pedersen, *Appl. Catal., B*, 2020, **279**, 119384.
76 A. J. Göttle and M. T. M. Koper, *J. Am. Chem. Soc.*, 2018, **140**, 4826–4834.
77 X. Min and M. W. Kanan, *J. Am. Chem. Soc.*, 2015, **137**, 4701–4708.
78 K. M. Waldie, F. M. Brunner and C. P. Kubiak, *ACS Sustainable Chem. Eng.*, 2018, **6**, 6841–6848.
79 Y. Y. Birdja, J. Shen and M. T. M. Koper, *Catal. Today*, 2017, **288**, 37–47.
80 C. Ye, S. J. Raaijman, X. Chen and M. T. M. Koper, *ACS Appl. Mater. Inter.*, 2022, **14**, 45263–45271.
81 O. Koga, T. Matsuo, H. Yamazaki and Y. Hori, *Advances in Chemical Conversions for Mitigating Carbon Dioxide*, 1998, vol. 114, pp. 569–572.
82 X. Liu, J. Xiao, H. Peng, X. Hong, K. Chan and J. K. Nørskov, *Nat. Commun.*, 2017, **8**, 15438.
83 J. D. Goodpaster, A. T. Bell and M. Head-Gordon, *J. Phys. Chem. Lett.*, 2016, **7**, 1471–1477.
84 H. Peng, M. T. Tang, X. Liu, P. Schlexer Lamoureux, M. Bajdich and F. Abild-Pedersen, *Energy Environ. Sci.*, 2021, **14**, 473–482.
85 H. Xiao, T. Cheng, W. A. Goddard, III and R. Sundararaman, *J. Am. Chem. Soc.*, 2016, **138**, 483–486.
86 G. Kastlunger, L. Wang, N. Govindarajan, H. H. Heenen, S. Ringe, T. Jaramillo, C. Hahn and K. Chan, *ACS Catal.*, 2022, **12**, 4344–4357.
87 X. Liu, P. Schlexer, J. Xiao, Y. Ji, L. Wang, R. B. Sandberg, M. Tang, K. S. Brown, H. Peng, S. Ringe, C. Hahn, T. F. Jaramillo, J. K. Nørskov and K. Chan, *Nat. Commun.*, 2019, **10**, 32.
88 A. J. Bard, L. R. Faulkner and H. S. White, *Electrochemical methods: fundamentals and applications*, John Wiley & Sons, 2022.
89 A. Baz and A. Holewinski, *J. Catal.*, 2021, **397**, 233–244.
90 C. T. Campbell, *J. Catal.*, 2001, **204**, 520–524.
91 C. T. Campbell, *ACS Catal.*, 2017, **7**, 2770–2779.
92 C. A. Wolcott, A. J. Medford, F. Studt and C. T. Campbell, *J. Catal.*, 2015, **330**, 197–207.
93 B. L. Foley and A. Bhan, *J. Catal.*, 2020, **384**, 231–251.
94 M. Liu, Y. Pang, B. Zhang, P. De Luna, O. Voznyy, J. Xu, X. Zheng, C. T. Dinh, F. Fan, C. Cao, F. P. G. de Arquer, T. S. Safaei, A. Mepham, A. Klinkova, E. Kumacheva, T. Filleter, D. Sinton, S. O. Kelley and E. H. Sargent, *Nature*, 2016, **537**, 382–386.
95 Y. Chen, C. W. Li and M. W. Kanan, *J. Am. Chem. Soc.*, 2012, **134**, 19969–19972.
96 Y. Hori, A. Murata, K. Kikuchi and S. Suzuki, *J. Chem. Soc., Chem. Commun.*, 1987, 728–729, DOI: 10.1039/C39870000728.
97 X. Zhu, J. Huang and M. Eikerling, *ACS Catal.*, 2021, **11**, 14521–14532.
98 M. Cho, J. T. Song, S. Back, Y. Jung and J. Oh, *ACS Catal.*, 2018, **8**, 1178–1185.

99 A. Thevenon, A. Rosas-Hernández, A. M. Fontani Herreros, T. Agapie and J. C. Peters, *ACS Catal.*, 2021, **11**, 4530–4537.
100 L. Xiong, X. Zhang, H. Yuan, J. Wang, X. Yuan, Y. Lian, H. Jin, H. Sun, Z. Deng and D. Wang, *Angew. Chem.*, 2021, **133**, 2538–2548.
101 J. L. Hitt, Y. C. Li, S. Tao, Z. Yan, Y. Gao, S. J. L. Billinge and T. E. Mallouk, *Nat. Commun.*, 2021, **12**, 1114.
102 M. Zhu, R. Ye, K. Jin, N. Lazouski and K. Manthiram, *ACS Energy Lett.*, 2018, **3**, 1381–1386.
103 L. Sun, V. Reddu, S. Xi, C. Dai, Y. Sheng, T. Su, A. C. Fisher and X. Wang, *Adv. Energy Mater.*, 2022, **12**, 2202108.
104 S. Liu, H. B. Yang, S.-F. Hung, J. Ding, W. Cai, L. Liu, J. Gao, X. Li, X. Ren, Z. Kuang, Y. Huang, T. Zhang and B. Liu, *Angew. Chem., Int. Ed.*, 2020, **59**, 798–803.
105 X. Wang, S. Feng, W. Lu, Y. Zhao, S. Zheng, W. Zheng, X. Sang, L. Zheng, Y. Xie, Z. Li, B. Yang, L. Lei, S. Wang and Y. Hou, *Adv. Funct. Mater.*, 2021, **31**, 2104243.
106 W. Zheng, Y. Wang, L. Shuai, X. Wang, F. He, C. Lei, Z. Li, B. Yang, L. Lei, C. Yuan, M. Qiu, Y. Hou and X. Feng, *Adv. Funct. Mater.*, 2021, **31**, 2008146.
107 T. Li, C. Yang, J.-L. Luo and G. Zheng, *ACS Catal.*, 2019, **9**, 10440–10447.
108 G. S. Prakash, F. A. Viva and G. A. Olah, *J. Power Sources*, 2013, **223**, 68–73.
109 J. Zhang, T. Fan, P. Huang, X. Lian, Y. Guo, Z. Chen and X. Yi, *Adv. Funct. Mater.*, 2022, **32**, 2113075.
110 E. L. Clark, S. Ringe, M. Tang, A. Walton, C. Hahn, T. F. Jaramillo, K. Chan and A. T. Bell, *ACS Catal.*, 2019, **9**, 4006–4014.
111 N. Hoshi, M. Kato and Y. Hori, *J. Electroanal. Chem.*, 1997, **440**, 283–286.
112 T. Hatsukade, K. P. Kuhl, E. R. Cave, D. N. Abram and T. F. Jaramillo, *Phys. Chem. Chem. Phys.*, 2014, **16**, 13814–13819.
113 M. R. Singh, Y. Kwon, Y. Lum, J. W. Ager, III and A. T. Bell, *J. Am. Chem. Soc.*, 2016, **138**, 13006–13012.
114 E. L. Clark, J. Resasco, A. Landers, J. Lin, L.-T. Chung, A. Walton, C. Hahn, T. F. Jaramillo and A. T. Bell, *ACS Catal.*, 2018, **8**, 6560–6570.
115 A. A. Peterson and J. K. Nørskov, *J. Phys. Chem. Lett.*, 2012, **3**, 251–258.
116 F. Abild-Pedersen, J. Greeley, F. Studt, J. Rossmeisl, T. R. Munter, P. G. Moses, E. Skúlason, T. Bligaard and J. K. Nørskov, *Phys. Rev. Lett.*, 2007, **99**, 016105.
117 J. Pérez-Ramírez and N. López, *Nat. Catal.*, 2019, **2**, 971–976.
118 M. L. Pegis, C. F. Wise, B. Koronkiewicz and J. M. Mayer, *J. Am. Chem. Soc.*, 2017, **139**, 11000–11003.
119 Y. Li and Q. Sun, *Adv. Energy Mater.*, 2016, **6**, 1600463.
120 D.-H. Nam, P. De Luna, A. Rosas-Hernández, A. Thevenon, F. Li, T. Agapie, J. C. Peters, O. Shekhah, M. Eddaoudi and E. H. Sargent, *Nat. Mater.*, 2020, **19**, 266–276.
121 Z. Cao, J. S. Derrick, J. Xu, R. Gao, M. Gong, E. M. Nichols, P. T. Smith, X. Liu, X. Wen, C. Copéret and C. J. Chang, *Angew. Chem., Int. Ed.*, 2018, **57**, 4981–4985.
122 S. Ahn, K. Klyukin, R. J. Wakeham, J. A. Rudd, A. R. Lewis, S. Alexander, F. Carla, V. Alexandrov and E. Andreoli, *ACS Catal.*, 2018, **8**, 4132–4142.
123 Y. Fang and J. C. Flake, *J. Am. Chem. Soc.*, 2017, **139**, 3399–3405.
124 Z. Cao, D. Kim, D. Hong, Y. Yu, J. Xu, S. Lin, X. Wen, E. M. Nichols, K. Jeong, J. A. Reimer, P. Yang and C. J. Chang, *J. Am. Chem. Soc.*, 2016, **138**, 8120–8125.
125 R. Reske, H. Mistry, F. Behafarid, B. Roldan Cuenya and P. Strasser, *J. Am. Chem. Soc.*, 2014, **136**, 6978–6986.
126 Z. Han, D. Han, Z. Chen, J. Gao, G. Jiang, X. Wang, S. Lyu, Y. Guo, C. Geng, L. Yin, Z. Weng and Q.-H. Yang, *Nat. Commun.*, 2022, **13**, 3158.
127 X. F. Lu, H. A. Ahsaine, B. Dereli, A. T. Garcia-Esparza, M. Reinhard, T. Shinagawa, D. X. Li, K. Adil, M. R. Tchalala, T. Kroll, M. Eddaoudi, D. Sokaras, L. Cavallo and K. Takanabe, *ACS Catal.*, 2021, **11**, 6499–6509.
128 Z.-W. Yang, J.-M. Chen, L.-Q. Qiu, W.-J. Xie and L.-N. He, *Angew. Chem., Int. Ed.*, 2022, **61**, e202205301.
129 J. S. Zeng, N. Corbin, K. Williams and K. Manthiram, *ACS Catal.*, 2020, **10**, 4326–4336.
130 A. Wuttig, Y. Yoon, J. Ryu and Y. Surendranath, *J. Am. Chem. Soc.*, 2017, **139**, 17109–17113.
131 S. Ringe, E. L. Clark, J. Resasco, A. Walton, B. Seger, A. T. Bell and K. Chan, *Energy Environ. Sci.*, 2019, **12**, 3001–3014.
132 A. Murata and Y. Hori, *Bull. Chem. Soc. Jpn.*, 1991, **64**, 123–127.
133 A. S. Malkani, J. Li, N. J. Oliveira, M. He, X. Chang, B. Xu and Q. Lu, *Sci. Adv.*, 2020, **6**, eabd2569.
134 L. Wang, S. A. Nitopi, E. Bertheussen, M. Orazov, C. G. Morales-Guio, X. Y. Liu, D. C. Higgins, K. R. Chan, J. K. Norskov, C. Hahn and T. F. Jaramillo, *ACS Catal.*, 2018, **8**, 7445–7454.
135 J. Li, K. Chang, H. Zhang, M. He, W. A. Goddard, J. G. Chen, M.-J. Cheng and Q. Lu, *ACS Catal.*, 2019, **9**, 4709–4718.
136 J. Li, X. Chang, H. Zhang, A. S. Malkani, M.-J. Cheng, B. Xu and Q. Lu, *Nat. Commun.*, 2021, **12**, 1–11.
137 X. Chang, J. Li, H. Xiong, H. Zhang, Y. Xu, H. Xiao, Q. Lu and B. Xu, *Angew. Chem., Int. Ed.*, 2022, **61**, e202111167.
138 H. Shen, Y. Wang, T. Chakraborty, G. Zhou, C. Wang, X. Fu, Y. Wang, J. Zhang, C. Li and F. Xu, *ACS Catal.*, 2022, **12**, 5275–5283.
139 J. Hou, X. Chang, J. Li, B. Xu and Q. Lu, *J. Am. Chem. Soc.*, 2022, **144**, 22202–22211.
140 X. Fu, Y. Wang, H. Shen, Y. Yu, F. Xu, G. Zhou, W. Xie, R. Qin, C. Dun, C. W. Pao, J. L. Chen, Y. Liu, J. Guo, Q. Yue, J. J. Urban, C. Wang and Y. Kang, *Mater. Today Phys.*, 2021, **19**, 100418.
141 Y. Zheng, A. Vasileff, X. Zhou, Y. Jiao, M. Jaroniec and S.-Z. Qiao, *J. Am. Chem. Soc.*, 2019, **141**, 7646–7659.
142 M. Schreier, Y. Yoon, M. N. Jackson and Y. Surendranath, *Angew. Chem., Int. Ed.*, 2018, **57**, 10221–10225.
143 O. Koga, Y. Watanabe, M. Tanizaki and Y. Hori, *Electrochim. Acta*, 2001, **46**, 3083–3090.
144 T. Burdyny and W. A. Smith, *Energy Environ. Sci.*, 2019, **12**, 1442–1453.
145 X. Lu, T. Shinagawa and K. Takanabe, *ACS Catal.*, 2023, **13**, 1791–1803.

146 A. C. Lausche, A. J. Medford, T. S. Khan, Y. Xu, T. Bligaard, F. Abild-Pedersen, J. K. Nørskov and F. Studt, *J. Catal.*, 2013, **307**, 275–282.
147 P. Hollins and J. Pritchard, *Surf. Sci.*, 1979, **89**, 486–495.
148 R. B. Sandberg, J. H. Montoya, K. Chan and J. K. Nørskov, *Surf. Sci.*, 2016, **654**, 56–62.
149 M. Jouny, G. S. Hutchings and F. Jiao, *Nat. Catal.*, 2019, **2**, 1062–1070.
150 M. Jouny, W. Luc and F. Jiao, *Nat. Catal.*, 2018, **1**, 748–755.
151 X. Wang, Y. Jiao, L. Li, Y. Zheng and S.-Z. Qiao, *Angew. Chem., Int. Ed.*, 2022, **61**, e202114253.
152 S. Narayanaru, J. Chinnaiah, K. L. Phani and F. Scholz, *Electrochim. Acta*, 2018, **264**, 269–274.
153 F. Che, J. T. Gray, S. Ha, N. Kruse, S. L. Scott and J.-S. McEwen, *ACS Catal.*, 2018, **8**, 5153–5174.
154 J. H. Montoya, C. Shi, K. Chan and J. K. Nørskov, *J. Phys. Chem. Lett.*, 2015, **6**, 2032–2037.
155 Y. Lum, T. Cheng, W. A. Goddard, III and J. W. Ager, *J. Am. Chem. Soc.*, 2018, **140**, 9337–9340.
156 K. Obata and F. F. Abdi, *Sustainable Energy Fuels*, 2021, **5**, 3791–3801.
157 Y. Lin, C. Deng, L. Wu, Y. Zhang, C. Chen, W. Ma and J. Zhao, *Energy Environ. Sci.*, 2020, **13**, 2602–2617.
158 G. Liu, W. S. Y. Wong, M. Kraft, J. W. Ager, D. Vollmer and R. Xu, *Chem. Soc. Rev.*, 2021, **50**, 10674–10699.
159 C. Balzarek, T. J. R. Weakley and D. R. Tyler, *J. Am. Chem. Soc.*, 2000, **122**, 9427–9434.
160 W. H. Bernskoetter, E. Lobkovsky and P. J. Chirik, *J. Am. Chem. Soc.*, 2005, **127**, 14051–14061.
161 P. Hauwert, R. Boerleider, S. Warsink, J. J. Weigand and C. J. Elsevier, *J. Am. Chem. Soc.*, 2010, **132**, 16900–16910.
162 C. L. Perrin, T. J. Dwyer and P. Baine, *J. Am. Chem. Soc.*, 1994, **116**, 4044–4049.
163 S. E. Scheppele, *Chem. Rev.*, 1972, **72**, 511–532.
164 M. Gómez-Gallego and M. A. Sierra, *Chem. Rev.*, 2011, **111**, 4857–4963.
165 W. Deng, P. Zhang, B. Seger and J. Gong, *Nat. Commun.*, 2022, **13**, 803.
166 X. Tian, P. Zhao and W. Sheng, *Adv. Mater.*, 2019, **31**, 1808066.
167 Y. Pocker and D. W. Bjorkquist, *J. Am. Chem. Soc.*, 1977, **99**, 6537–6543.
168 E. D. German and M. Sheintuch, *J. Phys. Chem. C*, 2010, **114**, 3089–3097.
169 W. Ma, S. Xie, X.-G. Zhang, F. Sun, J. Kang, Z. Jiang, Q. Zhang, D.-Y. Wu and Y. Wang, *Nat. Commun.*, 2019, **10**, 892.
170 W. Ma, S. Xie, T. Liu, Q. Fan, J. Ye, F. Sun, Z. Jiang, Q. Zhang, J. Cheng and Y. Wang, *Nat. Catal.*, 2020, **3**, 478–487.
171 X. Guo, S.-M. Xu, H. Zhou, Y. Ren, R. Ge, M. Xu, L. Zheng, X. Kong, M. Shao, Z. Li and H. Duan, *ACS Catal.*, 2022, **12**, 10551–10559.
172 S. Dey, T. K. Todorova, M. Fontecave and V. Mougel, *Angew. Chem., Int. Ed.*, 2020, **59**, 15726–15733.
173 A. Khadhraoui, P. Gotico, W. Leibl, Z. Halime and A. Aukauloo, *ChemSusChem*, 2021, **14**, 1308–1315.
174 K. Saihara, Y. Yoshimura, S. Ohta and A. Shimizu, *Sci. Rep.*, 2015, **5**, 10619.
175 A. Verma, J. P. Stoppelman and J. G. McDaniel, *Int. J. Mol. Sci.*, 2020, **21**, 403.
176 C. Ma, A. Laaksonen, C. Liu, X. Lu and X. Ji, *Chem. Soc. Rev.*, 2018, **47**, 8685–8720.
177 S. E. Tignor, T. W. Shaw and A. B. Bocarsly, *Dalton Trans.*, 2019, **48**, 12730–12737.
178 Y. Liu and C. C. L. McCrory, *Nat. Commun.*, 2019, **10**, 1683.
179 R. Wang, X. Wang, W. Weng, Y. Yao, P. Kidkhunthod, C. Wang, Y. Hou and J. Guo, *Angew. Chem., Int. Ed.*, 2022, **61**, e202115503.
180 J. Chen, M. Zhu, J. Li, J. Xu and Y.-F. Han, *J. Phys. Chem. C*, 2020, **124**, 16501–16507.
181 E. J. Dufek, T. E. Lister and M. E. McIlwain, *J. Appl. Electrochem.*, 2011, **41**, 623–631.
182 S. M. A. Kriescher, K. Kugler, S. S. Hosseiny, Y. Gendel and M. Wessling, *Electrochem. Commun.*, 2015, **50**, 64–68.
183 B. Endrődi, G. Bencsik, F. Darvas, R. Jones, K. Rajeshwar and C. Janáky, *Prog. Energy Combust. Sci.*, 2017, **62**, 133–154.
184 H. Yoshio, K. Katsuhei, M. Akira and S. Shin, *Chem. Lett.*, 1986, 897–898.
185 S. T. Ahn, I. Abu-Baker and G. T. R. Palmore, *Catal. Today*, 2017, **288**, 24–29.
186 M. Azuma, K. Hashimoto, M. Hiramoto, M. Watanabe and T. Sakata, *J. Electrochem. Soc.*, 1990, **137**, 1772.
187 T. Mizuno, K. Ohta, M. Kawamoto and A. Saji, *Energy Sources*, 1997, **19**, 249–257.
188 A. Löwe, C. Rieg, T. Hierlemann, N. Salas, D. Kopljar, N. Wagner and E. Klemm, *ChemElectroChem*, 2019, **6**, 4497–4506.
189 Z. Yin, H. Peng, X. Wei, H. Zhou, J. Gong, M. Huai, L. Xiao, G. Wang, J. Lu and L. Zhuang, *Energy Environ. Sci.*, 2019, **12**, 2455–2462.
190 J. Wei, X. Jian, C. Wu, S. Zhang and C. Yan, *J. Membr. Sci.*, 2005, **256**, 116–121.
191 J. Wang, G. Chen and S. Song, *Electrochim. Acta*, 2020, **330**, 135322.
192 Shalu, S. K. Chaurasia, R. K. Singh and S. Chandra, *J. Phys. Chem. B*, 2013, **117**, 897–906.
193 M. Chandesris, V. Médeau, N. Guillet, S. Chelghoum, D. Thoby and F. Fouda-Onana, *Int. J. Hydrogen Energy*, 2015, **40**, 1353–1366.
194 J.-B. Vennekötter, T. Scheuermann, R. Sengpiel and M. Wessling, *J. CO2 Util.*, 2019, **32**, 202–213.
195 D. Kim, W. Choi, H. W. Lee, S. Y. Lee, Y. Choi, D. K. Lee, W. Kim, J. Na, U. Lee, Y. J. Hwang and D. H. Won, *ACS Energy Lett.*, 2021, **6**, 3488–3495.
196 R. E. Vos and M. T. M. Koper, *ChemElectroChem*, 2022, **9**, e202200239.
197 H. H. Heenen, H. Shin, G. Kastlunger, S. Overa, J. A. Gauthier, F. Jiao and K. Chan, *Energy Environ. Sci.*, 2022, **15**, 3978–3990.
198 O. Christensen, S. Zhao, Z. Sun, A. Bagger, J. V. Lauritsen, S. U. Pedersen, K. Daasbjerg and J. Rossmeisl, *ACS Catal.*, 2022, **12**, 15737–15749.

199 E. Bertheussen, T. V. Hogg, Y. Abghoui, A. K. Engstfeld, I. Chorkendorff and I. E. L. Stephens, *ACS Energy Lett.*, 2018, **3**, 634–640.
200 D. S. Ripatti, T. R. Veltman and M. W. Kanan, *Joule*, 2019, **3**, 240–256.
201 D. Salvatore and C. P. Berlinguette, *ACS Energy Lett.*, 2019, **5**, 215–220.
202 S. Anantharaj and S. Noda, *J. Mater. Chem. A*, 2022, **10**, 9348–9354.
203 Y. Hori, A. Murata and R. Takahashi, *J. Chem. Soc., Faraday Trans. 1*, 1989, **85**, 2309–2326.
204 A. R. Heenan, J. Hamonnet and A. T. Marshall, *ACS Energy Lett.*, 2022, **7**, 2357–2361.
205 P. Grosse, D. Gao, F. Scholten, I. Sinev, H. Mistry and B. Roldan Cuenya, *Angew. Chem., Int. Ed.*, 2018, **57**, 6192–6197.
206 S. Popović, M. Smiljanić, P. Jovanovič, J. Vavra, R. Buonsanti and N. Hodnik, *Angew. Chem., Int. Ed.*, 2020, **59**, 14736–14746.
207 P. Sebastián-Pascual, S. Mezzavilla, I. E. L. Stephens and M. Escudero-Escribano, *ChemCatChem*, 2019, **11**, 3626–3645.
208 J. Vavra, T.-H. Shen, D. Stoian, V. Tileli and R. Buonsanti, *Angew. Chem., Int. Ed.*, 2021, **60**, 1347–1354.
209 X. Wang, K. Klingan, M. Klingenhof, T. Möller, J. Ferreira de Araújo, I. Martens, A. Bagger, S. Jiang, J. Rossmeisl, H. Dau and P. Strasser, *Nat. Commun.*, 2021, **12**, 794.
210 H. Jung, S. Y. Lee, C. W. Lee, M. K. Cho, D. H. Won, C. Kim, H.-S. Oh, B. K. Min and Y. J. Hwang, *J. Am. Chem. Soc.*, 2019, **141**, 4624–4633.
211 W. Zheng, J. Yang, H. Chen, Y. Hou, Q. Wang, M. Gu, F. He, Y. Xia, Z. Xia, Z. Li, B. Yang, L. Lei, C. Yuan, Q. He, M. Qiu and X. Feng, *Adv. Funct. Mater.*, 2020, **30**, 1907658.
212 D. Ren, Y. Deng, A. D. Handoko, C. S. Chen, S. Malkhandi and B. S. Yeo, *ACS Catal.*, 2015, **5**, 2814–2821.
213 B. Mei, C. Liu, J. Li, S. Gu, X. Du, S. Lu, F. Song, W. Xu and Z. Jiang, *J. Energy Chem.*, 2022, **64**, 1–7.
214 A. Zhang, Y. Liang, H. Li, B. Zhang, Z. Liu, Q. Chang, H. Zhang, C.-F. Zhu, Z. Geng, W. Zhu and J. Zeng, *Nano Lett.*, 2020, **20**, 8229–8235.
215 X. Wu, Y. Guo, Z. Sun, F. Xie, D. Guan, J. Dai, F. Yu, Z. Hu, Y.-C. Huang, C.-W. Pao, J.-L. Chen, W. Zhou and Z. Shao, *Nat. Commun.*, 2021, **12**, 660.
216 B. Qin, Y. Li, H. Wang, G. Yang, Y. Cao, H. Yu, Q. Zhang, H. Liang and F. Peng, *Nano Energy*, 2019, **60**, 43–51.
217 B. Huang, K. H. Myint, Y. Wang, Y. Zhang, R. R. Rao, J. Sun, S. Muy, Y. Katayama, J. Corchado Garcia and D. Fraggedakis, *J. Phys. Chem. C*, 2021, **125**, 4397–4411.
218 G. Hussain, L. Pérez-Martínez, J.-B. Le, M. Papasizza, G. Cabello, J. Cheng and A. Cuesta, *Electrochim. Acta*, 2019, **327**, 135055.
219 S. Ringe, E. L. Clark, J. Resasco, A. Walton, B. Seger, A. T. Bell and K. Chan, *Energy Environ. Sci.*, 2019, **12**, 3001–3014.
220 J. Li, D. Wu, A. S. Malkani, X. Chang, M.-J. Cheng, B. Xu and Q. Lu, *Angew. Chem., Int. Ed.*, 2020, **59**, 4464–4469.
221 M. C. O. Monteiro, F. Dattila, B. Hagedoorn, R. García-Muelas, N. López and M. T. M. Koper, *Nat. Catal.*, 2021, **4**, 654–662.
222 G. Marcandalli, M. C. O. Monteiro, A. Goyal and M. T. M. Koper, *Acc. Chem. Res.*, 2022, **55**, 1900–1911.
223 A. Goyal, G. Marcandalli, V. A. Mints and M. T. M. Koper, *J. Am. Chem. Soc.*, 2020, **142**, 4154–4161.
224 M. C. O. Monteiro, F. Dattila, N. López and M. T. M. Koper, *J. Am. Chem. Soc.*, 2022, **144**, 1589–1602.
225 A. Goyal, G. Marcandalli, V. A. Mints and M. T. Koper, *J. Am. Chem. Soc.*, 2020, **142**, 4154–4161.
226 C. J. Bondue, M. Graf, A. Goyal and M. T. Koper, *J. Am. Chem. Soc.*, 2020, **143**, 279–285.
227 J. Li, X. Li, C. M. Gunathunge and M. M. Waegele, *Proc. Natl. Acad. Sci. U. S. A.*, 2019, **116**, 9220–9229.
228 X. Lu, C. Zhu, Z. Wu, J. Xuan, J. S. Francisco and H. Wang, *J. Am. Chem. Soc.*, 2020, **142**, 15438–15444.
229 H. H. Bauer, *J. Electroanal. Chem. Interfacial Electrochem.*, 1968, **16**, 419–432.
230 J.-M. Savéant and D. Tessier, *Faraday Discuss. Chem. Soc.*, 1982, **74**, 57–72.
231 J. T. Hupp, H. Y. Liu, J. K. Farmer, T. Gennett and M. J. Weaver, *J. Electroanal. Chem. Interfacial Electrochem.*, 1984, **168**, 313–334.
232 J. N. Soderberg, A. C. Co, A. H. C. Sirk and V. I. Birss, *J. Phys. Chem. B*, 2006, **110**, 10401–10410.
233 A. T. Marshall and L. Vaisson-Béthune, *Electrochem. Commun.*, 2015, **61**, 23–26.
234 Y. J. Sa, C. W. Lee, S. Y. Lee, J. Na, U. Lee and Y. J. Hwang, *Chem. Soc. Rev.*, 2020, **49**, 6632–6665.
235 J. A. Gauthier, S. Ringe, C. F. Dickens, A. J. Garza, A. T. Bell, M. Head-Gordon, J. K. Nørskov and K. Chan, *ACS Catal.*, 2019, **9**, 920–931.
236 X. Zhang and Z. Zhou, *J. Phys. Chem. C*, 2022, **126**, 3820–3829.
237 A. A. Peterson, F. Abild-Pedersen, F. Studt, J. Rossmeisl and J. K. Nørskov, *Energy Environ. Sci.*, 2010, **3**, 1311–1315.
238 X. Zhao and Y. Liu, *J. Am. Chem. Soc.*, 2020, **142**, 5773–5777.
239 Y. Basdogan, A. M. Maldonado and J. A. Keith, *Wiley Interdiscip. Rev.: Comput. Mol. Sci.*, 2020, **10**, e1446.
240 X. Hu, S. Yao, L. Chen, X. Zhang, M. Jiao, Z. Lu and Z. Zhou, *J. Mater. Chem. A*, 2021, **9**, 23515–23521.
241 J.-B. Le, Q.-Y. Fan, J.-Q. Li and J. Cheng, *Sci. Adv.*, 2020, **6**, eabb1219.
242 S. Naserifar and W. A. Goddard, *Proc. Natl. Acad. Sci. U. S. A.*, 2019, **116**, 1998–2003.
243 S. Naserifar, Y. Chen, S. Kwon, H. Xiao and W. A. Goddard, *Matter*, 2021, **4**, 195–216.
244 L. Chen, X. Zhang, A. Chen, S. Yao, X. Hu and Z. Zhou, *Chin. J. Catal.*, 2022, **43**, 11–32.
245 A. Chen, X. Zhang and Z. Zhou, *InfoMat*, 2020, **2**, 553–576.
246 O. van der Heijden, S. Park, J. J. J. Eggebeen and M. T. M. Koper, *Angew. Chem., Int. Ed.*, 2023, **62**, e202216477.
247 Y. C. Li, D. Zhou, Z. Yan, R. H. Gonçalves, D. A. Salvatore, C. P. Berlinguette and T. E. Mallouk, *ACS Energy Lett.*, 2016, **1**, 1149–1153.
248 K. P. Kuhl, E. R. Cave, D. N. Abram and T. F. Jaramillo, *Energy Environ. Sci.*, 2012, **5**, 7050–7059.
249 Y. Zhao, X. Chang, A. S. Malkani, X. Yang, L. Thompson, F. Jiao and B. Xu, *J. Am. Chem. Soc.*, 2020, **142**, 9735–9743.

250 X. Chang, Y. Zhao and B. Xu, *ACS Catal.*, 2020, **10**, 13737–13747.
251 A. S. Malkani, M. Dunwell and B. Xu, *ACS Catal.*, 2019, **9**, 474–478.
252 A. Eilert, F. Cavalca, F. S. Roberts, J. R. Osterwalder, C. Liu, M. Favaro, E. J. Crumlin, H. Ogasawara, D. Friebel and L. G. Pettersson, *J. Phys. Chem. Lett.*, 2017, **8**, 285–290.
253 B. Hasa, M. Jouny, B. H. Ko, B. Xu and F. Jiao, *Angew. Chem., Int. Ed.*, 2021, **60**, 3277–3282.
254 S. Bhandari, S. Rangarajan and M. Mavrikakis, *Acc. Chem. Res.*, 2020, **53**, 1893–1904.
255 J. Resasco, F. Abild-Pedersen, C. Hahn, Z. Bao, M. T. M. Koper and T. F. Jaramillo, *Nat. Catal.*, 2022, **5**, 374–381.
256 P. Hutchison, C. J. Kaminsky, Y. Surendranath and S. Hammes-Schiffer, *ACS Central Sci.*, 2023, **9**, 927–936.
257 S. Oh, J. R. Gallagher, J. T. Miller and Y. Surendranath, *J. Am. Chem. Soc.*, 2016, **138**, 1820–1823.